REVIEW

Atomic level insights into metal halide perovskite materials by scanning tunneling microscopy and spectroscopy

Wei Zhang,[a] Luis K. Ono,[a] Jiamin Xue,[b] and Yabing Qi*[a]

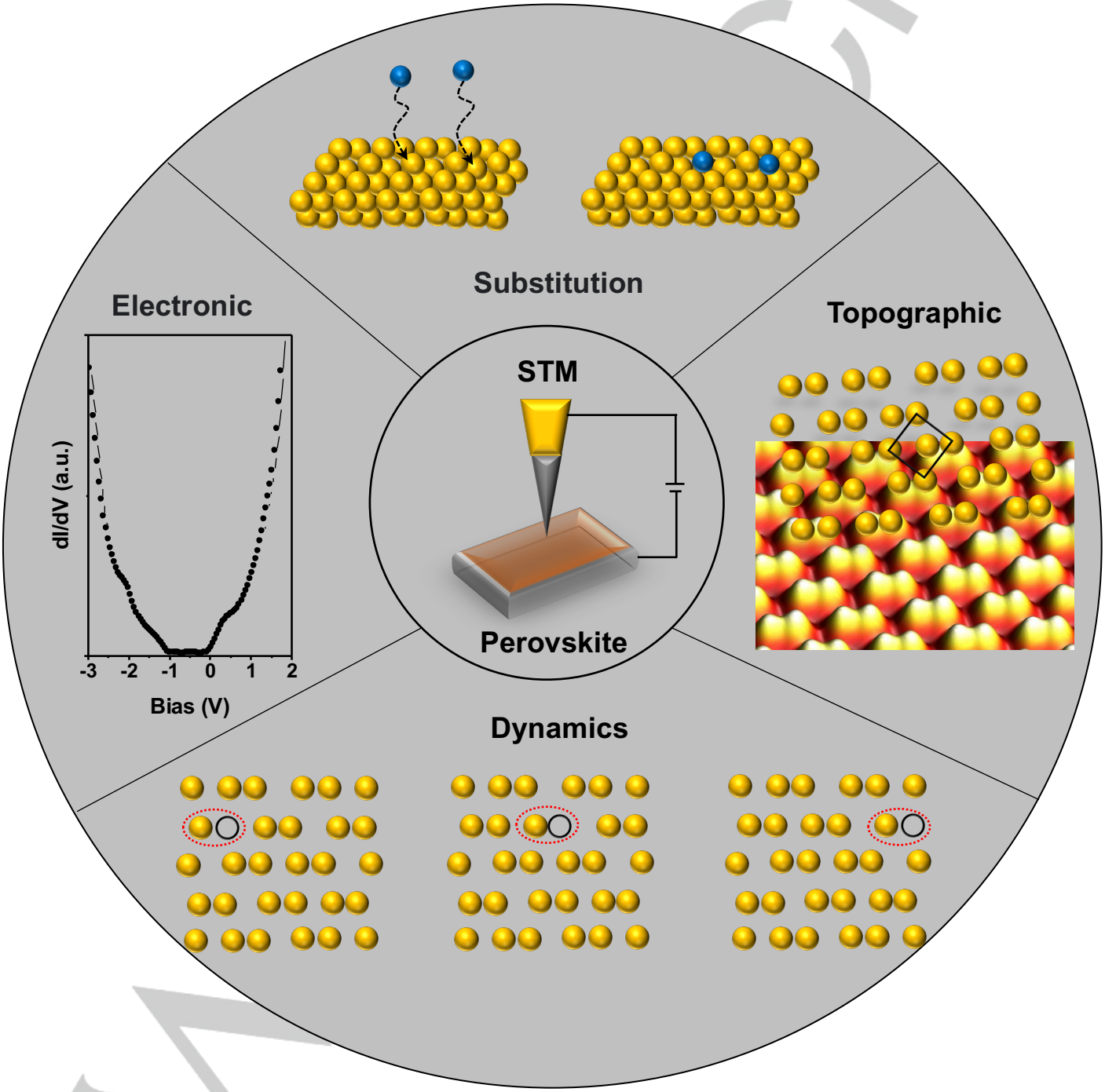

[a] Dr. W. Zhang, Dr. L. K. Ono, Prof. Y. B. Qi*
Energy Materials and Surface Sciences Unit (EMSSU), Okinawa
Institute of Science and Technology Graduate University (OIST)
1919-1 Tancha, Onna-son, Kunigami-gun, Okinawa 904-0495, Japan.
*Corresponding author: Yabing Qi, E-mail: Yabing.Qi@OIST.jp
[b] Prof. J. Xue
School of Physical Science and Technology
ShanghaiTech University
Shanghai 201210, China.

Abstract: Metal halide perovskite materials (MHPMs) have attracted significant attention because of their superior optoelectronic properties and versatile applications. The power conversion efficiency of MHPMs solar cells (PSCs) has skyrocketed to 25.5% nowadays. Although the performance of PSCs is already competitive, several important challenges still need to be solved to realize commercial applications. A thorough understanding of surface atomic structures and structure-property relationship is at the heart of these remaining issues. Scanning tunneling microscopy (STM) can be used to characterize the surface properties of MHPMs, which can offer crucial insights into MHPMs at the atomic scale. This paper reviews the recent progress of STM studies on MHPMs focusing on the underlying surface properties. We provide the understanding from the comparative perspective of a number of MHPMs. Also, we highlight a series of novel phenomena observed by STM. Finally, we outline a few research topics of primary importance for future studies.

1. Introduction

The early works on metal halide perovskite materials (MHPMs) can be dated back to 1893.[1] However, the interest in the perovskite materials was still rather limited at that time. It was until 2009 when MHPMs were used as a visible photosensitizer material in dye-sensitized solar cells,[2] MHPMs began to attract the attention of the scientific community. MHPMs have the perovskite crystal structure with a stoichiometry of ABX_3. The crystal structure consists of a 12-fold coordinated A cation occupying the site in the middle of the cube, which is surrounded by 8 corner-sharing $[BX_6]^{4-}$ octahedra. The possible selections of A, B and X site ions are governed by the Goldschmidt tolerance factor,[3] which is an empirical rule for predicting the stability and lattice distortion derived from a close-packing of spherical hard ions. In general terms, the A-site is typically occupied by an organic or inorganic monovalent cation, such as $CH_3NH_3^+$ (MA^+), $CH(NH_2)_2^+$ (FA^+), Cs^+ or a mixture of these cations; the B-site is occupied by a divalent metal cation, such as Pb^{2+}, Sn^{2+}, Ge^{2+} or a mixture of these cations; the X-site is occupied by a monovalent halide anion, such as I^-, Br^-, Cl^- or a mixture thereof.[4] Due to their excellent properties, MHPMs have emerged as a class of semiconductors with a broad range of applications, such as photovoltaics[4a, 4d, 4e, 5] photodetectors,[4j, 6] light-emitting diodes[7] and lasers.[8] Recently, the power conversion efficiency (PCE) of PSCs has skyrocketed from the initial 3.81% to 25.5%, which is approaching the record of crystalline silicon solar cells (26.1%).[9] Although the performance of PSCs is already competitive, several important challenges will still need to be solved to realize commercial applications, such as inadequate stability and reproducibility,[4i, 10] upscalable fabrication,[11] and potential concerns about toxic lead leakage during operation.[12] A thorough understanding of surface atomic structures and structure-property relationship is at the heart of these remaining issues.[13] The chemistry and physics at the interfaces presented in the complex architecture of PSCs have a profound impact on device performance (in terms of both PCE and stability). Despite the research on device applications of MHPMs has reached an impressive level, the fundamental understanding about this interesting class of materials is somewhere lagging behind at this stage, in particular regarding the atomic-level insights into the surface and interface properties and their influences on device stability and performance.

In general, the morphologies and compositions of perovskite materials are often characterized using the techniques such as X-ray diffraction (XRD), scanning electron microscopy (SEM) and transmission electron microscopy (TEM). Unfortunately, these techniques either lack atomic-level spatial resolution in real space and/or may cause severe damage to the MHPMs as the result of high-energy electron bombardment.[14] Scanning tunneling microscopy (STM), which is based on the quantum mechanical effect of tunneling, is a powerful tool that can be used to characterize the surface topographic and electronic properties of specimens with atomic resolution in real space. When a metal tip approaches a sample surface within a few angstroms, the tip and sample wave functions overlap together, the electron has a non-zero probability to jump through the barrier. Once a small bias voltage is applied, a tunneling current (typically nanoamperes) will be generated between them. This tunneling current is a function of the height of the tip relative to the surface and the local density of states at the sample surface. One of the advantages of STM is that it does not cause damage to the sample due to the negligible tunneling current and non-physical contact. Because of the unique operation principle, STM shows powerful capabilities in many aspects. For example, STM can probe the topography of the surface and interface with atomic resolution. It also allows *in situ* real-time monitoring and characterization of material growth and evolution processes, surface dynamics and surface chemistry. Scanning tunneling spectroscopy (STS) can precisely reveal the electronic structures of the surface at the atomic scale. Furthermore, STM can be combined with many other UHV techniques to provide a comprehensive picture of the sample surface. Compared with transmission electron microscopy (another powerful technique with the capability of atomic resolution imaging), STM experiments can be considered non-invasive and the sample preparation is relatively straightforward. However, STM requires an atomically smooth and conductive surface and a sharp metallic tip. Although STM can offer crucial insights into fundamental understanding of materials at the ultimate atomic scale[15], STM studies of perovskite materials are rare, presumably because of the technically difficulty in obtaining an immaculate and atomically flat surface.[13a, 16] Recent findings indicate that the surface trap states in the perovskite layer can

strongly influence the performance of the solar cell devices,[7b, 17] however, the chemical and physical properties of atomic-scale defects and surface and interface properties are not well-understood. The investigation into the surface phase transitions, surface defect dynamics, ion migration and halide-substitution of MHPMs is still in its infancy.

In this review, we first summarize the methods to prepare high-quality MHPMs for STM characterization. We then elucidate the basic properties of perovskite crystal surfaces, including atomic-scale topography, surface electronic properties, surface phase transitions, surface defect dynamics, halide substitution enhanced stability and interfacial structures. Finally, considering the impact of the surface and interface on device performance, we propose a few future research directions focusing on the studies of properties of metal halide perovskite absorbers based on STM.

Yabing Qi is Professor and Unit Director of Energy Materials and Surface Sciences Unit at Okinawa Institute of Science and Technology Graduate University in Japan, and a Fellow of the Royal Society of Chemistry. Prof. Qi received his B.S., M.Phil., and Ph.D. from Nanjing University, Hong Kong University of Science and Technology, and UC Berkeley, respectively. His research interests include surface / interface sciences, perovskite solar cells, batteries, organic electronics, energy materials and devices (https://groups.oist.jp/emssu).

2. Sample preparation

An atomically flat surface with reasonable conductivity is key to successful STM studies, therefore the preparation of MHPMs is the first crucial step. To achieve STM characterization, considerable efforts have been devoted to development of different approaches to prepare or synthesize high quality perovskite thin films.[18] These approaches can be mainly classified as “cleavage” and “deposition”. The cleavage method applies a steady force to precisely cleave the bulk crystal for yielding a fresh crystal plane; the deposition method bases on the interaction of atoms or molecules with the substrate to form high quality thin films on the surface by heating the precursors under high vacuum.

2.1. Vacuum cleavage

Mechanical cleavage is commonly used to prepare and study a variety of single crystalline samples including inorganic semiconductors[19] and two-dimensional (2D) layered materials.[20] However, the tetragonal/cubic structure of MHPMs does not have an easy cleavable crystal plane.[21] Even though cleavage is non-trivial for MHPMs, several findings have been reported to overcome this barrier.[18c-e] Qi and coworkers succeeded in cleaving $MAPbBr_3$ single crystals with the remaining thickness of about 1-2 mm.[18e] A single crystal of $MAPbBr_3$ was mounted on a sample holder and cleaved with a scalpel paralleling to one of the facets of the crystal inside the ultra-high vacuum (UHV) chamber, as depicted in Figure 1a. For some particular samples such as $Sr_3Ru_2O_7$ and Sr_2RuO_4 oxide-type perovskites, the cleavage process does not generate intrinsic defects, which is explained by the high formation energies of 4.19 eV and 3.81 eV for the Sr and O vacancies, respectively.[22] As comparison, the formation energies for the Br and MA vacancies in $MAPbBr_3$ and I and MA vacancies in $MAPbI_3$ are relatively low in halide perovskites (Table 1), which have been reported in experimental and theoretical studies on halide perovskite surfaces.[18e, 18f, 22-23] In addition, the observed defects on as-cleaved surfaces may be caused by the bulk impurities.[22, 24] After a period of weeks under UHV and dark conditions, the fresh surface of $MAPbBr_3$ degrades and converts to $PbBr_2$.[18c] In addition, the $MAPbBr_3$ perovskite possesses a stable cubic phase at room temperature (RT) and the orthorhombic phase at a temperature below 144.5 K,[25] respectively. The step-height was determined as 6.0 ± 0.6 Å for the cubic and 5.3 ± 0.4 Å for the orthorhombic phases, respectively.[18c, 18e] The main reason for choosing bulk $MAPbBr_3$ single crystals as the sample is that it is easier to prepare compared to other MHPMs because of its relatively large crystal size and high stability.[18d] Generally, the preparation process of vacuum cleavage is non-trivial, but this method provides a feasible strategy to expose the clean interface and study the nature of the surface properties for MHPMs.

Table 1. Formation energies for the vacancies in metal halide perovskites in comparison with those in an oxide perovskite, Sr_2RuO_4.

$MAPbI_3$			$MAPbBr_3$			Sr_2RuO_4	
V_I	V_{MA}	V_{MAI}	V_{Br}	V_{MA}	V_{MABr}	V_{Sr}	V_O
0.08 eV[23a]	0.16 eV[23a]	0.23 eV[23b]	2.39 eV[23f]	3.32 eV[23f]	1.96 eV[23f]	4.19 eV[22]	3.81 eV[22]
0.29~0.87 eV[23c]	-0.02~1.06 eV[23c]	0.08 eV[23d]	-	-	1.94 eV[18f]	-	-
1.85 eV[23e]	1.94 eV[23e]	-	-	-	-	-	-

V_X represents an “X” vacancy defect.

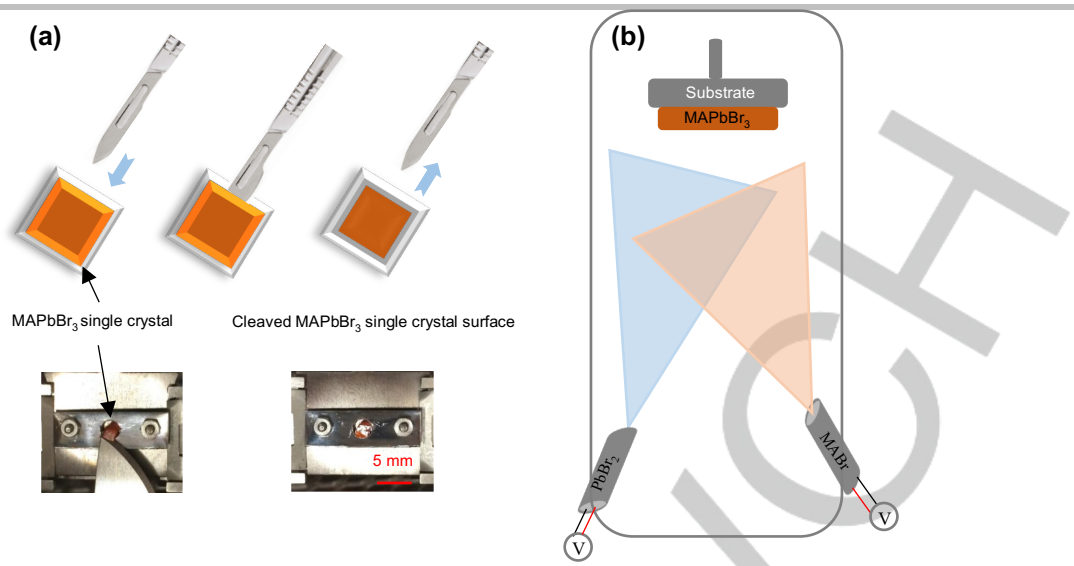

Figure 1. Illustration of sample preparation methods for STM. (a) The vacuum cleaving of a $MAPbBr_3$ single crystal. Adapted with permission from Ref.[18e]. Copyright 2015 American Chemical Society. (b) The dual-source vapor deposition set-up for $MAPbBr_3$ films. Adapted with permission from Ref.[18h]. Copyright 2014 The Royal Society of Chemistry

2.2. Vacuum vapor deposition

The vacuum vapor deposition method is one of the suitable techniques for growing thin films, which has three advantages. First of all, it is performed in vacuum, so as-grown thin films have a high purity. Secondly, the films are grown at a controllable deposition rate, which is beneficial to ensure uniformity of thin film properties. Thirdly, it usually leads to a smooth surface. Generally, an effective deposition process only occurs in a thermodynamically nonequilibrium state,[26] which is strongly dependent on the free surface energy of the substrate and the adatoms, as well as the interfacial energy between them.[27] In 2013, Snaith and co-workers succeeded in growing uniform flat thin $MAPbI_{3-x}Cl_x$ films with a thickness of approximately 330 nm on top of the compact TiO_2-coated fluorine-doped tin oxide (FTO)-coated glass surface by using the dual-source co-evaporation method at 10^{-5} mbar.[18g] Two crucibles were loaded with MAI and $PbCl_2$, respectively. Then the MAI source was heated to about 120°C, and $PbCl_2$ was heated to about 325°C.[18g] Qi and coworkers focused on the preparation of $MAPbX_3$ (X = Br or I)-based perovskite thin films via dual-source co-evaporation in an UHV environment,[18f, 18h-k] where for $MAPbBr_3$, the MABr and $PbBr_2$ molecules were evaporated at 361 and 498 K, respectively, for 10 min, and the clean Au(111) substrate was kept at 130 K during deposition in order to ensure the adhesion of the methylammonium molecules. The sample was then post-annealed at room temperature for 3 h. For $MAPbI_3$, the MAI and PbI_2 molecules were evaporated at 378 and 513 K, respectively, for 5 min, while the clean Au(111) substrate was kept at 130 K, and then the sample was post-annealed at room temperature over a period of approximately 120-180 min.[18j, 18k] Figure 1b shows an illustration of a dual-source thermal evaporation deposition set-up. By adjusting the evaporation time, $MAPbBr_3$ perovskite thin films with different thicknesses could be prepared. Zhong and coworkers prepared $MAPbI_3$ thin films on Au(111) surface by co-deposition of MAI and PbI_2 under UHV conditions.[18m, 18n] The height of the step edge of $MAPbI_3$ sheets is about 6.3 Å, which equals a half of the lattice constant of the orthorhombic $MAPbI_3$ in the *c* axis, indicating that these sheets consist of a monolayer thickness with atomically smooth surface.[29] As the deposition time was increased, a multilayer $MAPbI_3$ film was obtained with a final nominal thickness of 10.8 monolayers on top of the substrate.[18n] This layer-by-layer growth method with the well-defined surfaces allows the precise elucidation on the structure-property relationship and it is of crucial importance for the further development of MHPMs solar cells. $CsPbI_3$ and mixed halide perovskites such as $MAPbBr_{3-y}I_y$, $MAPbBr_{3-z}Cl_z$ and $MAPbI_{3-x}Cl_x$ can be fabricated by vacuum deposition method as well. [18i, 18j, 18o] The $CsPbBr_3$ perovskite films could also be prepared by using single-source evaporation method.[18r] The different molar ratios of CsBr and $PbBr_2$ powders were mixed and pressed into tablets as precursors. The TiO_2-coated FTO-coated glass substrate was maintained at 300°C, and simultaneously rotated during the deposition to obtain good homogeneity of $CsPbBr_3$ thin films. A triple-cation $Cs_{0.5}FA_{0.4}MA_{0.1}Pb(I_{0.83}Br_{0.17})_3$ perovskite films were grown on the tin-doped indium oxide (ITO) coated glass substrate by using simultaneous multiple-source thermal evaporation where the precursors were kept at ~425°C for CsBr, ~100°C for MAI, ~165°C for FAI and ~295°C for PbI_2, respectively.[30] Incorporation of inorganic Cs^+ into MHPMs for forming multiple cation configurations is a common strategy to improve the performance with better reproducibility and stability as well as higher efficiencies.[10a, 31] The vacuum vapor deposition method could provide highly controllable thin perovskite films with a high quality, uniform morphology and possibly reduced impurities and defects.

3. Characterization by the STM-based techniques

3.1. Atomic-scale characterizations of various metal halide perovskite materials

The surface structures of MHPMs have been modelled by theoretical computations, and the surface reconstructions usually originate from the instability of the surface layer induced by perpendicular macroscopic polarization.[32] Typically, the polar surface would be compensated by the surface reconstruction, which thus results in depolarization and the formation of the final stabilized layer. STM can be employed to determine the surface structures with high spatial resolution, which provides valuable insights into fundamental understanding of perovskite materials.

a) $MAPbBr_3$

Qi and coworkers successfully achieved the first atomic-level STM imaging of a vacuum cleaved $MAPbBr_3$ single crystal surface.[18e] Since the STM measurements were performed at 4.5 K, the cleaved crystal exhibited the orthorhombic structure, and the lattice constant was calculated to be 7.87 Å × 12.02 Å × 8.79 Å.[33] A flat and smooth $MAPbBr_3$ terrace was observed with a step height of half of the unit cell of $MAPbBr_3$. High-resolution STM images displayed the superlattice structure with two types of surface reconstruction configurations. As shown in Figure 2a and b, the bright protrusions could be distinguished to the zigzag and dimer patterns. Both patterns co-existed in certain areas of the surfaces (see Figure 2c), which corresponded to MABr-terminated surface based on first-principles density functional theory (DFT) calculations. Moreover, the PbBr-terminated (001) surface was also observed by STM, showing a 2 × 2-like rectangular pattern (Figure 2d).[18d] The STM measurements indicated that a few small areas were covered by the zigzag structure and the prevalent structure is the dimer structure, which covered the majority of the surface.[18d, 18f, 18i] In addition, the dominant dimer structures tended to take <110> as the preferential directions. In contrast, the zigzag structures were formed by the zigzag rows of Br anions preferably along the [100] direction.[18d] With the support of DFT calculations, the bright protrusions were assigned to Br anions on the corner of the $PbBr_6$ octahedra for the MABr-terminated (001) surface of the orthorhombic crystal. These two distinct types of surface structures could be interpreted as two different in-plane orientation configurations of the MA cations. As presented in Figure 2e and f, the zigzag structure was associated with a perpendicular arrangement of the MA cations, resulting in a non-zero net dipole moment, while the dimer structure was associated with an anti-parallel arrangement of the MA cations with a zero net dipole moment within the plane of the surface. The simulated STM images (Figure 2e and f) were in good agreement with the experimental STM images (Figure 2a and b). Because of the strong electrostatic interaction between the MA cations and Br anions, when the MA cations were reoriented within the plane of the surface, the Br anions would relax in another lower energy state, which might alter the position of the Br lattice. This is consistent with the results measured by the line profiles (Figure 2g). A reorientation event was observed in the same row and this phenomenon is discussed in more detail in Section 3.3. In addition to the observed Br anions, the MA cations could be imaged with a reduced sample bias voltage (i.e., corresponding to a smaller tip-sample distance) (see Figure 2h), which showed the additional protrusions corresponding to the MA cations consistent with the calculation results (Figure 2i).

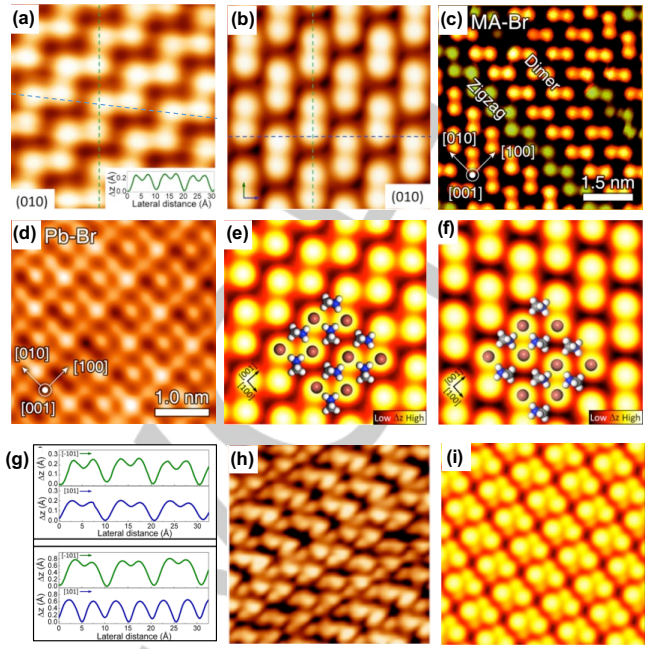

Figure 2. Atomic-scale characterizations of the $MAPbBr_3$ perovskite (001) surface. (a) High-resolution STM image of zigzag surface structure (31 × 31 $Å^2$, U = −5 V and I = 0.1 nA). (b) High-resolution STM image of the dimer surface structure (31 × 31 $Å^2$, U = −9 V and I = 0.1 nA). Panels (a,b) were reprinted with permission from Ref.[18e]. Copyright 2015 American Chemical Society. (c) The two surface structures co-existing on the same terrace (U = −5.5 V and I = 0.2 nA). (d) High-resolution STM image of the PbBr-terminated (001) surface (U = −5.5 V and I = 0.2 nA). Panels (c,d) were reprinted with permission from Ref.[18d]. Copyright 2019 American Chemical Society. (e, f) Simulated STM images of the zigzag and dimer structures. Br and MA ions were overlaid. (g) Line profiles along the dashed lines in (a) and (b) for the two different observed zigzag (top) and dimer (bottom) structures. (h) High-resolution STM image of the MABr-terminated (001) surface under a low bias voltage (42 × 42 $Å^2$, U = −3 V and I = 0.1 nA). (i) Simulated STM image of the MABr-terminated (001) surface with a smaller tip-sample distance. Panels (e-i) were reprinted with permission from Ref.[18e]. Copyright 2015 American Chemical Society.

b) $MAPbI_3$

Zhong and coworkers revealed the surface structures of an ultrathin $MAPbI_3$ film by STM and DFT calculations.[18m, 18n] The $MAPbI_3$ films were grown on Au(111) surface by dual-source co-evaporation and subsequent *in situ* STM experiments were carried out at 78 K. The model of the orthorhombic $MAPbI_3$ unit cell was shown in Figure 3a. The large-scale STM image showed that the flat $MAPbI_3$ films were formed on top of the Au(111) surface with a continuous sheet size of 100 nm (Figure 3b). The height step was 6.3 Å extracted from the STM image as shown in Figure 3c equal to one-half of the lattice constant in the *c*-axis. In the high-resolution images of Figure 3d and e, the zigzag and dimer structures can be clearly distinguished, where the lattice constants extracted from the STM image were a = 8.8 ± 0.2 Å and b = 8.5 ± 0.2 Å with a subtle height difference (see the height profile in Figure 3f). This result is consistent with the experimental structure obtained by XRD.[29] It can also be observed that two distinct structures were formed on the same terrace, where the dimer structure covered the majority of the surface, indicating that the dimer structure was stabler than the zigzag one because the total energy per unit cell is reduced by ~34 meV in the case of the dimer structure.[18m] Complementary DFT calculations indicated that the bright spots corresponded to the iodine anions at the MAI-terminated (001) surface. Similar results were reported by Qi and coworkers in their investigation of the CuPc-$MAPbI_3$ interface structures,[18k] which will be discussed in more detail below in Section 3.6.

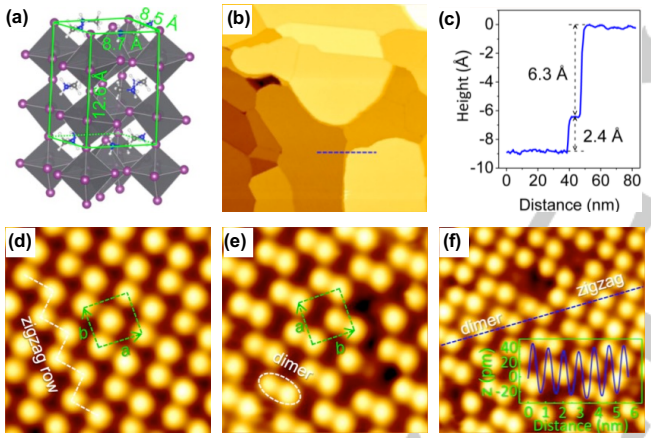

Figure 3. STM characterizations of the $MAPbI_3$ thin films. (a) Crystal structure of the orthorhombic $MAPbI_3$ perovskite. (b) Large-scale STM image of the $MAPbI_3$ perovskite film surface (300 × 300 nm^2, U = 2.5 V and I = 30 pA). (c) Height profile along the dashed line in (b). (d-f) High-resolution STM images of the zigzag and dimer structures (43 × 43 $Å^2$, U = 2.5 V and I = 50 pA), and two structures coexisting in the same terrace (56 × 56 $Å^2$, U = 2.5 V and I = 50 pA). The unit cells were highlighted by dashed rectangles. Inset in (f): The height profile revealed a height difference less than 10 pm. All panels were reproduced with permission from Ref.[18m]. Copyright 2016 American Chemical Society.

c) Mixed-halide perovskites

Mixing halide compositions in the MHPMs have a significant impact on their properties and stability.[34] It has been reported that the incorporation of a small amount of Cl in MHPMs can improve the stability,[35] extend carrier recombination lifetime[36] and increase open circuit voltage.[37] However, only a few studies have explored the surfaces of mixed halide perovskites,[38] and the role of Cl in MHPMs remains elusive.[39] In this case, direct characterization of the precise location of the incorporated Cl in mixed perovskites is the best way to clarify these issues. Qi and coworkers conducted STM investigations by incorporating a small amount of different types of halogen ions, I or Cl, into $MAPbBr_3$ to unravel the role of halogen in the mixed halide perovskite.[18i] The high-resolution STM images revealed the MA-halogen surface terminations for the (001) surface of the pristine $MAPbBr_3$, $MAPbBr_{3-y}I_y$ and $MAPbBr_{3-z}Cl_z$ mixed-halide perovskites (Figure 4a, b and c). The STM topography images revealed the bright and dark protrusions accompanied by different apparent heights and widths, which were different from the pristine $MAPbBr_3$ surface where all Br anions had the same height and width (Figure 4d). The apparent height of the bright protrusions was 40 ± 10 pm higher than the surrounding Br ions, while they were also larger in diameter, according to the line profile (Figure 4e). In contrast, the dark protrusions were 20 ± 10 pm lower than the neighboring Br ions (see Figure 4f). These bright protrusions were assigned to I anions due to their larger ionic radius than Br anions, and the dark protrusions were assigned to the Cl anions due to the smaller ionic radius. Noteworthily, these bright or dark protrusions were randomly distributed on the surface. Complementary information gained from the fast Fourier transform (FFT) of the STM images clearly revealed a quasi-square unit cell that was consistent with the (001) plane of the orthorhombic structure. The FFTs of STM images for $MAPbBr_{3-y}I_y$ and $MAPbBr_{3-z}Cl_z$ were similar to the pristine $MAPbBr_3$ indicating no surface structure change, in agreement with theoretical calculations.[38b, 40] The calculation results indicated that the substitution of Br by I (or Cl) is energetically favorable, and the corresponding simulated STM images exactly duplicated the results observed in the experiment (Figure 4g, h and i), especially that the height differences of I and Cl ions relative to Br ions were calculated to be +0.35 Å and −0.24 Å, respectively. These values are in good agreement with the STM measurements.

Qi and coworkers revealed the atomic scale surface structure of the mixed-halide perovskite $MAPbI_{3-x}Cl_x$.[18j] In addition to the I-I dimers, Cl-I pairs with different heights and widths can also be distinguished (Figure 4j). The average height of incorporated Cl ions is ~0.7 Å lower than the neighboring I ions, as shown in Figure 4k and l. Unlike the case of the incorporation of Cl ions into the $MAPbBr_3$ perovskite, Cl-Cl dimers were also observed in $MAPbI_{3-x}Cl_x$, indicating that the Cl-Cl dimer had a total energy rather close to that of the Cl-I dimer, which was also confirmed by DFT calculations. Here three important points need to be emphasized: (1) the substitution reaction of I ion by Cl ion occurs not only in the dimer structure but also in the zigzag structure; (2) a certain amount of Cl ions can be mixed into $MAPbI_3$, but most of the Cl ions incorporated on the surface prefer to emerge near the grain boundaries rather than at the center of the grains, and this surface inhomogeneous phenomenon has been reported previously;[41] (3) Cl ions are incorporated in both the surface and sub-surface layers of $MAPbI_3$, which have a pronounced impact on electronic properties and stability of the $MAPbI_{3-x}Cl_x$ perovskite. These findings not only reveal the precise location of the Cl and I

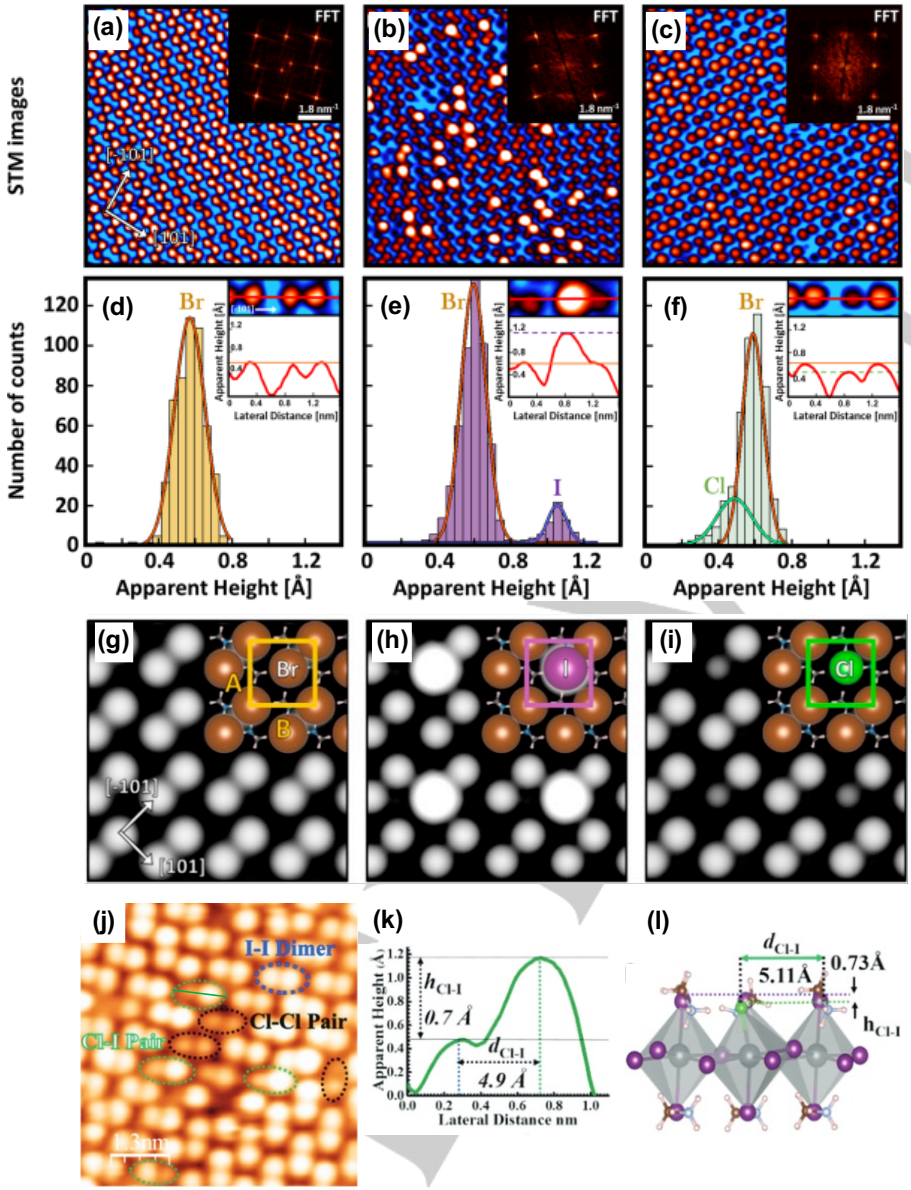

Figure 4. Detailed structural characterizations of mixed-halide perovskites. High-resolution STM images of (a) the pristine $MAPbBr_3$ surface (10 × 10 nm^2, U = 1.3 V and I = 80 pA), (b) the $MAPbBr_{3-y}I_y$ surface (10 × 10 nm^2, U = 2.0 V and I = 120 pA) and (c) the $MAPbBr_{3-z}Cl_z$ surface (10 × 10 nm^2, U = −2.0 V and I = 100 pA). The bright and dark protrusions were assigned to iodine and chlorine ions, respectively, which substitute Br ions at the surface. Inset: FFT images obtained from the corresponding topographic STM images. (d-f) Histogram of the apparent height distribution of the local maxima (i.e., the ions). The major peaks correspond to the Br ions, while the minor peaks are associated with iodine and chlorine ions, respectively. Inset: the typical profiles obtained for the different halides (Br, I, Cl) at the perovskite surface. (g-i) Calculated (001) surface of (g) pristine $MAPbBr_3$, (h) $MAPbBr_{3-y}I_y$ and (i) $MAPbBr_{3-z}Cl_z$. Inset: the corresponding surface model and unit cell. Panels (a-i) were reprinted with permission from Ref.[18i]. Copyright 2019 American Chemical Society. (j) High-resolution STM images of the $MAPbI_{3-x}Cl_x$ surface (14.5 × 14.5 nm^2, U = −2.5 V and I = 50 pA). (k) Line profile of the Cl-I pair along the green line in (j). (l) DFT model for the Cl-I pair with height and length. Panels (j-l) were reprinted with permission from Ref.[18j]. Copyright 2021 The Royal Society of Chemistry.

anions in the mixed halide perovskites but also provided an answer to the extent of their incorporation into the crystal lattice.

d) $CsPbBr_3$

All-inorganic metal halide perovskites show better stability than the organic-inorganic metal halide perovskites,[42] e.g., they can withstand the flux of electrons required for electron microscopy. Although high-angle annular dark field (HAADF) imaging by scanning transmission electron microscopy (STEM) revealed the surface structure of $CsPbBr_3$ single crystals with atomic resolution, the relatively weak signal of the Br-terminated CsPbBr3 surface led to the difficulty in observing the surface Br ions in detail.[43] Qi and coworkers for the first time reported the growth of ultrathin $CsPbBr_3$ films with a thickness of approximately 4 ± 1 nm on a clean Au(111) surface by dual-source evaporation.[18o] Similar to the organic-inorganic hybrid metal halide perovskites, two distinct surface rearrangement patterns co-existed on the same terrace.

These two domains were observed in four different orientations rotated ± 45° and ± 90° with respect to one another (see Figure 5a). To further understand these two different structures, the DFT calculations were carried out. The bright spots were assigned to the Br anions of the CsBr-terminated (001) surface of the orthorhombic crystal structure with the *Pnma* space group. Due to the lower density of states (DOS), the Cs cations could not be resolved in the STM images. Based on the STM observations and DFT calculations, the stripe pattern of the bright spots can be represented as a rectangular unit cell with the lattice constants of A = 7.3 Å, and B = 14 Å (Figure 5b).

Figure 5. Surface structure of the $CsPbBr_3$ perovskite. (a) Large-scale STM image of the $CsPbBr_3$ perovskite with the typical orientations of the stripe and armchair domains (29 × 12 nm^2, U = 2.17 V and I = 30 pA). Experimental high-resolution STM image (upper), simulated STM image (middle), and crystal structure model (lower) of (b) the stripe structure (3.9 × 2.8 nm^2, U = 2.3 V and I = 50 pA) and (c) armchair structure (5.2 × 4.2 nm^2, U = 2.0 V and I = 100 pA). Unit cells for both structures were marked in a rectangular and quasi-square shape, respectively. The lattice parameters were consistent with crystal structure model. Color code: Cs (green), Br (brown). All panels were reproduced with permission from Ref.[18o]. Copyright 2020 American Chemical Society.

In contrast, the armchair patterns consist of the alternation of bright and dark Br pair rows with the lattice parameters of c = 11.8 Å and d = 11.6 Å (Figure 5c) for the quasi-square unit cell. This alternating bright and dark surface reconstruction is caused by a change in the vertical position of the surface Br and Cs ions along the [101] direction (see Figure 5c). Interestingly, the spherically symmetric Cs^+ ion would not lead to the rearrangement of the surrounding Br^- ions due to its non-polar property. However, two distinct rearrangement patterns of the surface atoms can be distinguished clearly by STM. Moreover, the stripe structure is energetically more favorable than the armchair structure. This means that the stripe structure has higher surface stability than the armchair structure, which is consistent with the experimental observations that the stripe domains were found to be more abundant on the surface. Liang and coworkers revealed that the nonpolar CsBr-terminated (001) surface showed the best stability compared to the polar surface through DFT calculations.[44] This is consistent with the experimental observations by STEM and STM.

In the section above, we discuss the nature of the surface structures of MHPMs. In the next section, we focus on the electronic properties, which impact the performance of PSCs strongly.

3.2. Electronic structures and Fermi level position

Scanning tunneling spectroscopy (STS) is the method of choice to determine the local density of states (LDOS) at the surface. Ultraviolet photoemission spectroscopy (UPS) and inverse photoemission spectroscopy (IPES) can measure the energy positions of the valence band maximum (VBM) and conduction band minimum (CBM) at the surface of semiconductors. Figure 6a presents a typical STS dI/dV spectrum for cleaved $MAPbBr_3$ recorded at 4.5 K, which shows that the major contribution of LDOS originates from the occupied state, while the unoccupied state does not show an appreciable differential conductance.[18e] This is in good agreement with the partial density of states calculations, suggesting that the DOS is contributed by the orbitals of Br (major contribution) and the C and N of MA (minor contribution) (Figure 6b). Special attention should be paid to the surface reconstructions and the variation in their electronic properties. The LDOS of zigzag (ferroelectric) and dimer (antiferroelectric) domains exhibited a small difference in the energy positions of the orbitals (for details see the inset of Figure 6b). This small difference might have an impact on the local light-harvesting properties and interfacial coupling of perovskites.[18e] Figure 6c presents the dI/dV spectra of the cleaved $MAPbBr_3$ acquired at RT, revealing the different onset of the valence and

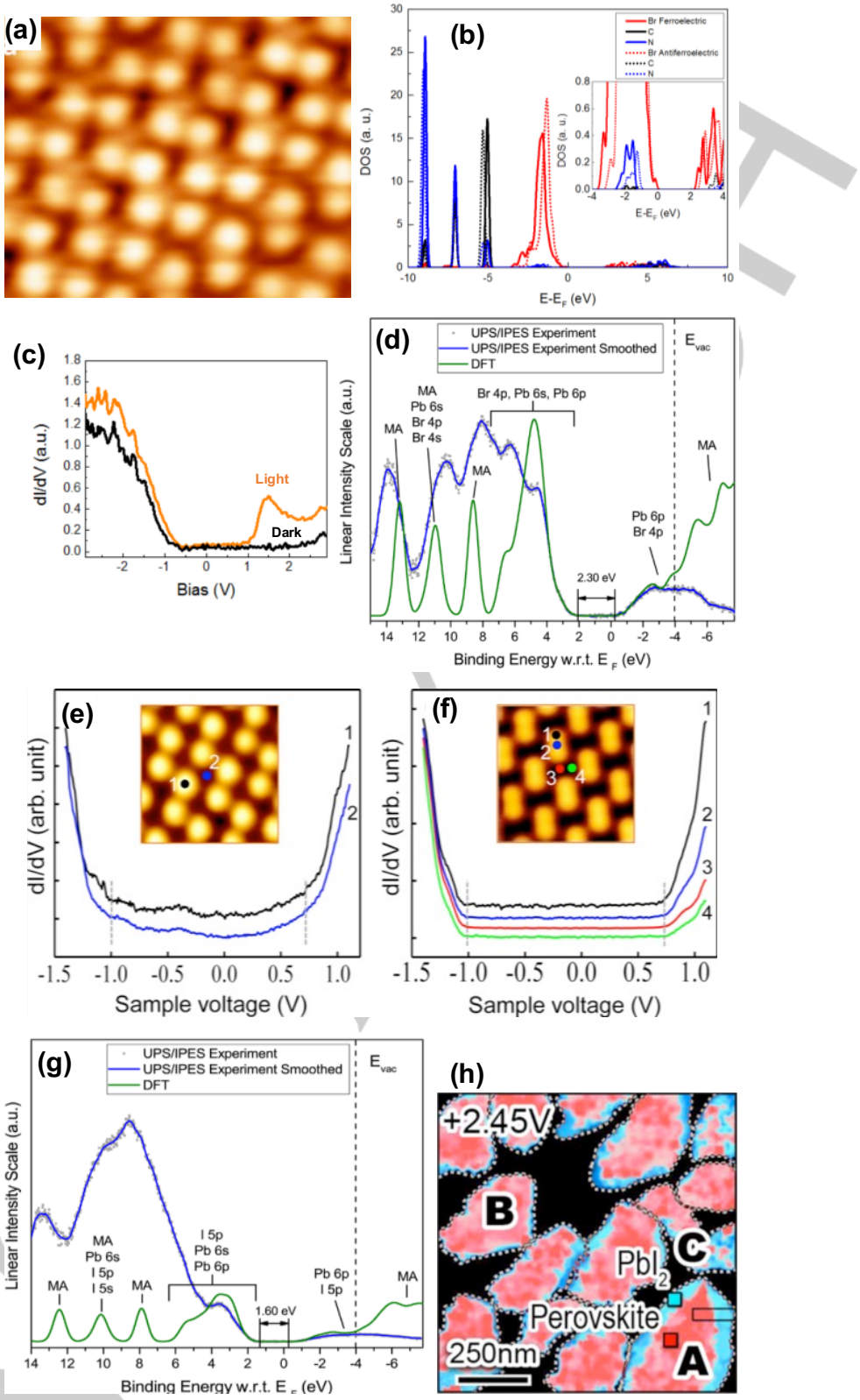

Figure 6. Electronic properties of perovskite materials. (a) dI/dV spectra on orthorhombic $MAPbBr_3$, obtained from forward and backward direction. Inset: Corresponding I(V) spectrum. (b) Comparison of density of states calculations on two different domains-polar (solid line) and non-polar (dotted line). Inset: Zoom of the energy region close to the Fermi level. (c) dI/dV spectra on cubic $MAPbBr_3$. The black line obtained in dark and orange line obtained under light irradiation. Panels (a-c) were reprinted with permission from Ref.[18e]. Copyright 2015 American Chemical Society. (d) UPS and IPES spectra of $MAPbBr_3$ with DFT simulations. Reprinted with permission from Ref.[45]. Copyright 2016 American Chemical Society. The typical dI/dV spectra of $MAPbI_3$ perovskite for (e) zigzag structure and (f) dimer structure, which were acquired from different sites as marked in the inset of the STM images. Panels (e,f) were reproduced with permission from Ref.[18m]. Copyright 2016 American Chemical Society. (g) UPS and IPES spectra of $MAPbI_3$ with DFT simulations. Reprinted with permission from Ref.[45]. Copyright 2016

American Chemical Society. (h) dI/dV mapping of $MAPbI_3$ perovskite (U = 2.45 V) with point-to-point electronic dI/dV curves. Reprinted with permission from Ref.[50d]. Copyright 2017 American Chemical Society.

conduction bands. A strong increase of the signal intensity was observed under light irradiation, indicating the generation of additional free charge carriers and tunneling channels.[18e] Endres et al. determined the band gap of $MAPbBr_3$ films on top of the TiO_2/FTO substrate to be 2.30 eV by a combination of UPS, IPES with DFT calculations.[45] The intensity peaks near the valence band were dominated by the contribution of Br 4p, with minor contributions from Pb 6s and 6p. For the unoccupied side, the bottom of the conduction band was dominated by the contribution of Pb 6p, with a minor contribution from Br 4p (Figure 6d).[45] This is similar to the results reported by Qi and coworkers[18e] excepting the Fermi level position in the band gap that was found to be closer to the conduction band (CB) side, which may be caused by the different sample preparation methods and the type of substrates.[46] In a separate measurement of angle-resolved *photoemission* spectroscopy (ARPES) on $MAPbBr_3$ single crystals, Fauster and coworkers demonstrated that the phase transition from the orthorhombic to the cubic structure would directly affect the surface electronic structure.[47] Interestingly, Rashba-splitting was detected not only in the orthorhombic but also in the cubic phase of $MAPbBr_3$,[47-48] which may arise from the surface polar reconstruction phenomenon or induced by strain.[13b, 49] The electronic structure of $MAPbI_3$ with the Fermi level position has been reported by several groups.[18m, 45-46, 50] Typical dI/dV spectra for deposited $MAPbI_3$ presented in Figure 6e and f were acquired at different sites of two types of surface structures.[18m] The position of CBM is at 0.7 eV above the Fermi level (V = 0), while the position of VBM is at 1.0 eV below the Fermi level. This is different from the onset of the lowest binding energy for the valence band (VB) obtained by ARPES in the range of 1.3-1.4 eV,[50a] probably due to substrate effects. The electronic gap of $MAPbI_3$ is about 1.7 eV, which is in good agreement with the UPS/IPES measurements[45, 50b] and photoluminescence (PL) measurements.[51]The DOS is mainly contributed by the orbitals of I and Pb (Figure 6g). On the basis of the STS measurements by Balberg and coworkers and Redinger and coworkers, the Fermi level position in the band gap of $MAPbI_3$ could be change by the different surface compositions of different synthesis routes.[46c, 50c] The surface inhomogeneities were revealed by the mapping image of the normalized dI/dV spectra, where two different types of local electronic signals were determined at the same crystal grains as shown in Figure 6h.[38c, 50d] The Fermi energy level positions of $MAPbI_3$ films were also influenced by the substrates.[46a, 46b]

A small amount of Cl incorporation would not change the band gap in the bulk of the parent perovskites, which has been confirmed by the UPS/IPES measurements and theoretical calculations.[18i, 38b, 50b] However, the work function of the mixed halide perovskite decreses after Cl substitution, but remains unchanged with iodide incorporation (Figure 7a).[18i] On the basis of the DFT calculations, the projected density of states (PDOS) of $MAPbBr_{3-y}I_y$ was contributed by the orbitals of Br and MA, as well as I 5p states, while $MAPbBr_{3-z}Cl_z$ was contributed by the orbitals of Br and MA, as well as Cl 3p states (Figure 7b).[18i] In contrast, incorporation of a certain amount of Cl or I ions would effectively modulate the electronic characteristic of mixed halide perovskites.[52] The UPS/IPES results showed an increased band gap of $MAPbI_{3-x}Cl_x$ perovskite after incorporation of a certain amount of Cl ions (see Figure 7c)[18j]. Moreover, a larger work function of $MAPbI_{3-x}Cl_x$ was also found compared to pristine $MAPbI_3$ by the UPS measurements, which was consistent with earlier UPS measurements performed by Kahn and coworkers.[50b]

The local electronic structure of the $CsPbBr_3$ perovskite was characterized by Qi and coworkers using STS taken on the Br ion of the stripe and armchair structure on the CsBr-terminated (001) surface.[53] Surprisingly, the representative normalized dI/dV spectra for these two distinct type domains were similar (see Figure 7d). A well-defined band gap of 2.5 eV was derived from the dI/dV spectra based on the VB and CB edges. This gap is 0.2 eV larger than the value measured in UPS-IPES measurements (Figure 7e).[18o, 45, 54] Based on the exact atomic structure of $CsPbBr_3$, DFT calculations were performed and revealed that the main contribution of the VBM originated from the Br 4p and Pb 6s orbitals, while the CBM was dominated by the Pb 6p and Br 4p orbitals, as shown in Figure 7e, in agreement with Kahn and coworkers.[45]

Recently, the LDOS of a mixed-cation lead halide perovskite of $MA_{0.83}FA_{0.17}PbI_3$ was studied by Nienhaus and coworkers, showing the normalized dI/dV spectra recorded in the positive forward direction and negative reverse direction with a band gap of 1.55 eV and 1.44 eV, respectively (Figure 7f), which was closer to the optical gap of 1.6 eV measured by PL experiments.[55] Interestingly, the sweep direction would affect the type of perovskites that an n-type character of $MA_{0.83}FA_{0.17}PbI_3$ was identified for the forward direction while a p-type character was identified for the reverse direction. Therefore, we can conclude that the type of perovskites is determined by the preparation methods, substrate effect and voltage sweep directions, which are summarized in Table 2. A better understanding of the electronic properties MHPMs is of paramount importance to improve perovskite solar cell performance.

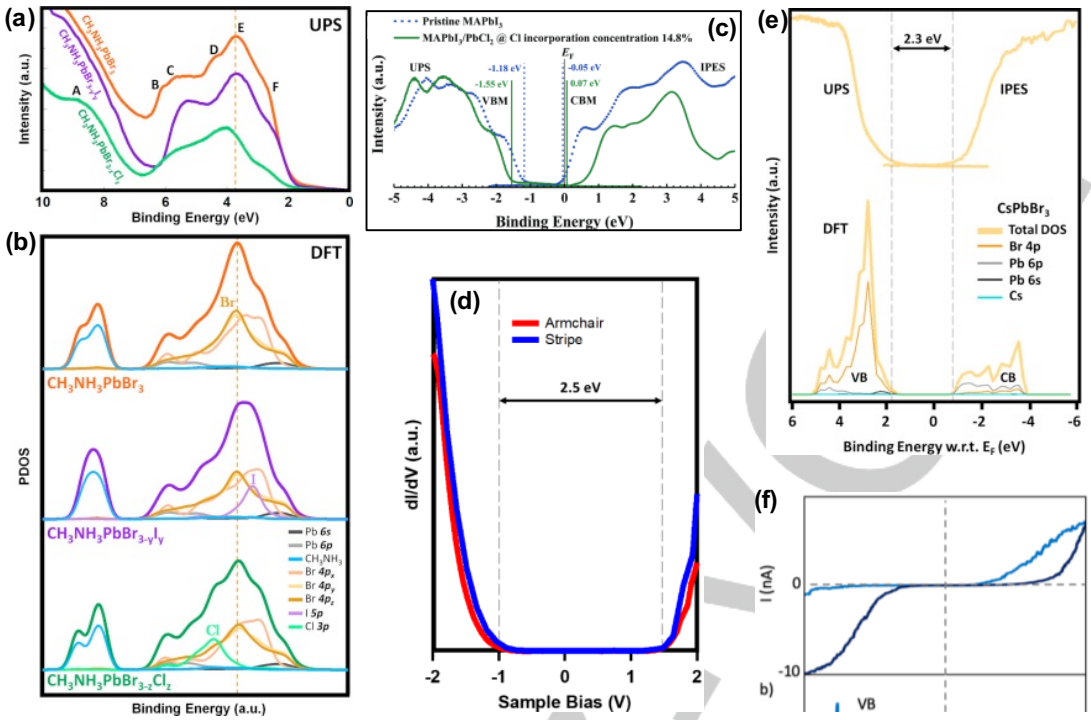

Figure 7. Determination of electronic properties. (a) Experimental UPS spectra of pure $MAPbBr_3$ (orange) and mixed $MAPbBr_{3-y}I_y$ (purple), $MAPbI_{3-x}Cl_x$ (green) perovskites. (b) Calculated PDOS of pure $MAPbBr_3$ (orange) and mixed $MAPbBr_{3-y}I_y$ (purple), $MAPbI_{3-x}Cl_x$ (green) perovskites. The different colored lines indicate different contributions of orbitals. Panels (a,b) were reproduced with permission from Ref.[18l]. Copyright 2019 American Chemical Society. (c) UPS/IPES spectra of pristine $MAPbI_3$ (dashed blue) and mixed $MAPbI_{3-x}Cl_x$ (solid green). Reproduced with permission from Ref.[18j]. Copyright 2021 The Royal Society of Chemistry. (d) dI/dV spectra of $CsPbBr_3$ perovskite for the stripe and armchair domains. (e) Electronic structure of $CsPbBr_3$ perovskite. Top: UPS-IPES spectra. Bottom: Calculated PDOS. The gray dashed line indicates the position of the valence band and conduction band edges. Panels (d,e) were reproduced with permission from Ref.[18o]. Copyright 2020 American Chemical Society. (f) dI/dV spectra of $MA_{0.83}FA_{0.17}PbI_3$ perovskite. Reproduced with permission from Ref.[55]. Copyright 2020 American Institute of Physics.

Table 2. Summary of the reported band gap values for MHPMs prepared by different methods and on different substrates.

Material	Method	Substrate	Type	Band gap (eV)					WF (eV)	ref
				STS	UPS/IPES	XPS E_F-E_{VBM}	DFT	Optical		
$MAPbBr_3$	Cleavage	Single crystal	p	~2.1	-	-	~2.3	-	-	[18e]
	Deposition	Au(111)	n	-	E_F-E_{VBM} = 1.70	-	-	~2.3	4.77	[18i]
	Solution	TiO_2/ITO	n	-	2.3	-	2.3	-	4.0	[45]
	Solution	TiO_2/FTO	n	-	2.3	-	-	-	4.0	[50b]
	Solution	PEDOT: PSS/ITO	n	-	2.3	-	~2.3	-	5.27	[46d]
$MAPbI_3$	Deposition	Au(111)	n	1.7	-	-	-	-	-	[18m]
	Solution	TiO_2/ITO	n	-	1.6	-	1.6	-	4.0	[45]
	Solution	glass	n	-	E_F-E_{VBM} = 1.43	-	-	1.62	4.21	[50i]
	Solution	Cu_2O	p	-	-	0.9	1.85	-	4.9	[46a]
		NiO	n	-	-	1.03		-	4.49	
		PEDOT:PSS	n	-	-	1.38		-	4.43	
		FTO	n	-	-	1.69		-	4.22	
		Al_2O_3	n	-	-	1.7		-	3.72	
		ZnO	n	-	-	1.72		-	4.64	
		TiO_2	n	-	-	1.72		-	4.03	

		ZrO_2	n	-	-	1.77		-	3.86	
	Solution	sNiO/ITO	p	-	1.7	-	-	-	4.7	[46b]
		TiO_2/ITO	n	-	1.7	-	-	-	4.0	
	Solution	TiO_2/FTO	n	-	1.7	-	-	-	3.99	[50b]
	Solution	ITO	n	1.58		-	-	-	-	[46c]
	Solution	TiO_2/FTO	p	1.53	-	-	-	1.60	-	[50c]
	Solution	TiO_2/FTO	n	1.50	-	-	-	-	-	[50d]
	Solution	PEDOT:PSS/ITO	n	-	1.7	-	-	-	4.7	[50e]
	Deposition	Au(111)	n	-	1.13	-	~1.2	-	5.07	[18j]
	Solution	microcrystal	n	-	E_F-E_{VBM} = 1.15	-		1.50	4.29	[50j]
	Solution	mp-TiO_2/FTO	n	-	E_F-E_{VBM} = 1.33	-	-	1.57	4.02	[50k]
	Solution	ITO	n	-	E_F-E_{VBM} =1.42	-	-	1.54	4.1	[50l]
	Solution	PEDOT: PSS/ITO	n	-	1.59	-	~1.6	-	4.42	[46d]
$MAPbBr_{3-y}I_y$	Deposition	Au(111)	n	-	E_F-E_{VBM} 1.80	-	<2.3	-	4.79	[18i]
$MAPbBr_{3-z}Cl_z$	Deposition	Au(111)	n	-	E_F-E_{VBM} = 1.65	-	~2.3	-	4.57	[18i]
$MAPbI_{3-x}Cl_x$	Solution	TiO_2/FTO	n	-	1.7	-	-	-	4.14	[50b]
	Deposition	Au(111)	n	-	1.62	-	~1.4	-	4.76	[18j]
$MAPbBr_3(Cl)$	Solution	TiO_2/FTO	-	-	-	-	-	-	4.5	[56]
	Solution	PEDOT:PSS/FTO	-	-	-	-	-	-	5.1	
$CsPbBr_3$	Deposition	Au(111)	p	2.5	2.3	-	2.3	-	4.72	[18o]
	Solution	TiO_2/ITO	n	-	2.3	-	2.3	-	4.1	[45]
	Solution	ZnO/ITO	p	-	E_F-E_{VBM} = ~1.1	-	-	2.37	4.7	[54a]
	Deposition	ITO	n	-	E_F-E_{VBM} = 1.75	-	-	2.33	3.98	[54b]
	Solution	ITO	-	-	E_F-E_{VBM} = 1.18	-	-	-	4.46	[54c]
$MA_{0.83}FA_{0.17}PbI_3$	Solution	ITO	n	1.55 (F)*	-	-	-	1.6	-	[55]
$MA_{0.83}FA_{0.17}PbI_3$	Solution	ITO	p	1.44 (R)*	-	-	-	1.6	-	[55]
$FA_{0.83}Cs_{0.17}PbI_3$	Solution	SnO_2/FTO	n	-	1.81	-	1.57	-	3.91	[4k]

E_F: Fermi level; E_{VBM}: valance-band maximum; WF: work function; ITO: indium-doped tin oxide; FTO: fluorine-doped tin oxide; PEDOT: PSS: poly (3, 4-ethylenedioxythiophene): polystyrene sulfonate; sNiO: sol–gel nickel oxide; mp-TiO_2: mesoporous-TiO_2; *F and R mean forward direction and reverse direction of the dI/dV spectra.

3.3. Surface structure transition under external stimuli

Using STM, the surface reconstruction behavior was observed for $MAPbBr_3$, $MAPbI_3$ and $CsPbBr_3$. The surface reorientation of Br dimers was revealed in sequential STM images for the deposited $MAPbBr_3$, where the Br dimer rotated by 90° relative to its original orientation (Figure 8a). This could be interpreted as the dissociation and re-association of the Br^- pair.[18f] The essential reason for this reorientation was the re-alignment of the dipole of the MA^+ group, arising from an in-plane rotation of MA^+ in response to electric field. The rotation of MA^+ led to the dissociation of the Br dimer and further rotation resulted in the formation of the new dimer structure with other neighboring Br ions (Figure 8b). Notably, $MAPbBr_3$ was kept at a low temperature range of 4.6 K-180 K for STM observations. Even at such low temperatures, the surface reorientation was still observed, indicating a low transition energy barrier. The calculations revealed that when Br^- and MA^+ moved together, the system energy did not change with a lower transition energy of 0.46 eV (Figure 8c).[18f] This suggests that the surface reorientation of Br dimer is reversible. Similar to the case of $MAPbBr_3$, two types of surface structures for $MAPbI_3$, the dimer and zigzag domains, can be reversibly transformed by applying a voltage pulse (Figure 8d-f).[18m] The phase transition energy barrier between two the distinct structural domains was calculated to be 0.18 eV per unit cell. The calculated value of the rotational barrier for the MA^+ cation was around 50 meV. This relatively low energy barrier means that the rotation can occur during STM operation, which is consistent with the previously reported studies.[57]

Besides external electrical stimuli, a photo-driven molecule dipole reordering of the cleaved $MAPbBr_3$ surface was reported by Chiu and coworkers.[18d] The (2 × 2) dimer structure on the MAI-terminated (001) face was observed in dark condition as presented in Figure 3e. This (2 × 2) dimer structure could be transformed into a new (4 × 2) surface structure under laser illumination (Figure 8g and h). This new (4 × 2) structure was related to the rearrangement of the MA cation dipole orientation. This phase transition was reversible, i.e., when the illumination was removed, the (2 × 2) dimer phase was reformed, indicating that the laser illumination did not decompose the MA cations. With the support of DFT calculations, the underlying mechanism is

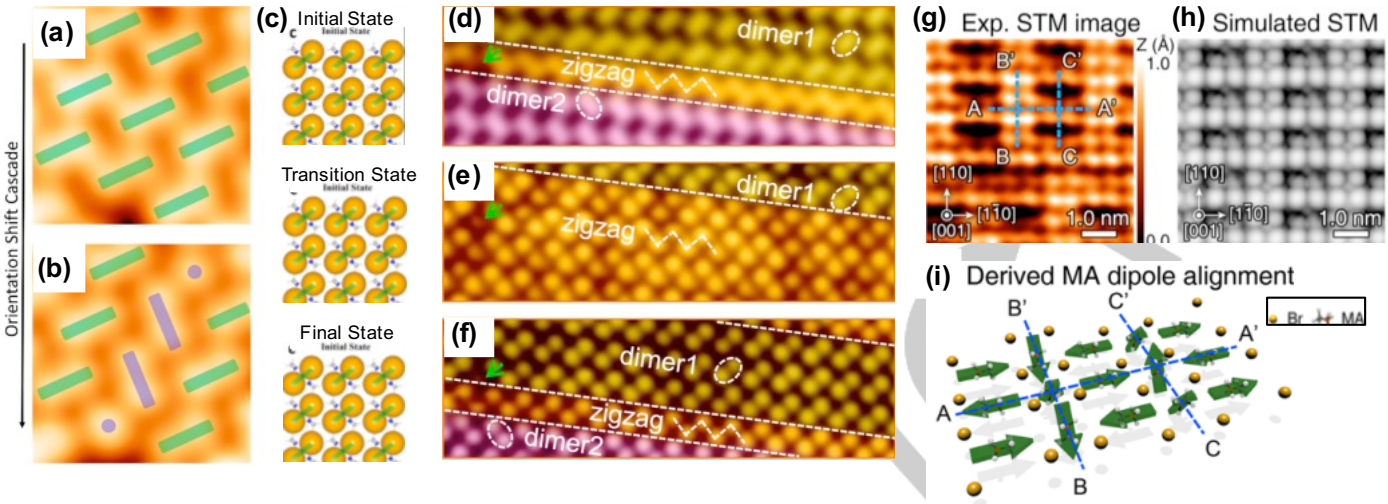

Figure 8. Surface reconstruction under external stimuli. (a, b) Consecutive STM images of the $MAPbBr_3$ perovskite, showing the dimer structure orientation shift (2.3 × 2.3 nm^2, U = −9.0 V and I = 20 pA). (c) Simulated dimer structure reorientation, including initial, transition, and final states. Color code: N (blue), C (gray), H (white), Br (brown). Panels (a-c) were reproduced with permission from Ref.[18f]. Copyright 2019 American Chemical Society. (d-f) Consecutive STM images of $MAPbI_3$ showing the reversible transition between the dimer and zigzag structures. d). U = 2.0 V, e). U = 0.85 V, and f). U = −1.25 V (4.2 × 12.8 nm^2, I = 30 pA). Panels (d-f) were reproduced with permission from Ref.[18m]. Copyright 2016 American Chemical Society. (g, h) Experimental and simulated STM images of (4 × 2) structure of $MAPbBr_3$ under laser illumination. (i) Model of the MA orientation pattern. Panels (g-i) were reproduced with permission from Ref.[18d]. Copyright 2019 American Chemical Society.

proposed to be a photo-driven separation of electron-hole pairs in spatially displaced orbitals, which generated polarization fields leading to the rearrangement of polarized MA cations, as illustrated in Figure 8i. The tilting of the MA^+ dipoles in the centers of the bright (B-B') and dark (C-C') stripes led to a change in the degree of dipole polarization, which in turn caused a difference in the repulsive or attractive force exerted on the Br ions. This difference resulted in the dipole negative siding up in the bright stripes (B-B') while the positive siding up in the dark stripes (C-C'). In addition, the dipoles between the MA^+ cations must be in-plane oriented and alternatingly point toward the B-B' and C-C' lines.

Although the two types of surface domains were observed on the CsBr-terminated (001) surface, the surface reorientation has not been observed for $CsPbBr_3$,[53] indicating a more stable surface structure probably because of the stronger Coulomb interactions.[58]

3.4. Surface defect dynamics

Recent findings suggested that the role of defects was crucial for the further development of PSCs, because they would have a direct impact on the structural stability, carrier recombination, and charge transfer properties.[7b, 17, 59] The nature and formation mechanism of point defects in MHPMs have been studied using DFT calculations.[23c, 23f, 60] However, the investigation of these point defects experimentally remains difficult, and so far only a very few studies have been reported on this topic.[18e, 18f, 18m, 59i] Recently, the atomic-scale surface structure of the deposited $MAPbBr_3$ was characterized in detail by Qi and coworkers *via* STM combined with DFT calculations (Figure 9a).[18f] Two distinct types of intrinsic point defects, unpaired Br anions and vacancies, were observed on the MABr-terminated (001) surface. The unpaired Br anion was frequently found in cases where there was a pair of mismatched orientations in the same row and they were isolated from each other (Figure 9b). In contrast, if there was a vacancy adjacent to the Br anions, two adjacent unpaired Br defects could be formed, as shown in Figure 9c. Various types of depression vacancies were observed, including single, double, and triple defects, as shown in Figure 9d-f, respectively. The DFT calculations showed that the formation of MABr vacancies was more energetically favorable compared to the Br anion vacancies. Similar results were also reported by Li and coworkers,[23f] where the simulated model (Figure 9g) and STM image (Figure 9h) are in good agreement with the STM experimental observations. For a single MABr vacancy, there is a MA cation nearby rotated 90° with the positive nitrogen end of the dipole near the unpaired Br anion (see Figure 9i), where the formation energy was calculated to be 1.94 eV for single MABr vacancies, 3.49 eV for double vacancies and 5.26 eV for triple MABr vacancies, respectively.[18f] The presence of vacancies assisted the migration of ions and when MABr ions migrated together in close proximity to a vacancy, a lower transition energy barrier was expected. Similar surface defects were also observed by Qi and coworkers[18e] and Zhong and coworkers[18m] for cleaved $MAPbBr_3$ and deposited $MAPbI_3$ perovskite films, respectively. Generally, mechanical cleavage does not create intrinsic defects,[22] while the deposited perovskite thin films often contain atomic-scale surface defects[18f, 18m, 18n].

Significantly, the surface vacancies could act as adsorption sites for oxygen or H_2O molecules, resulting in decomposition.[23f, 62]

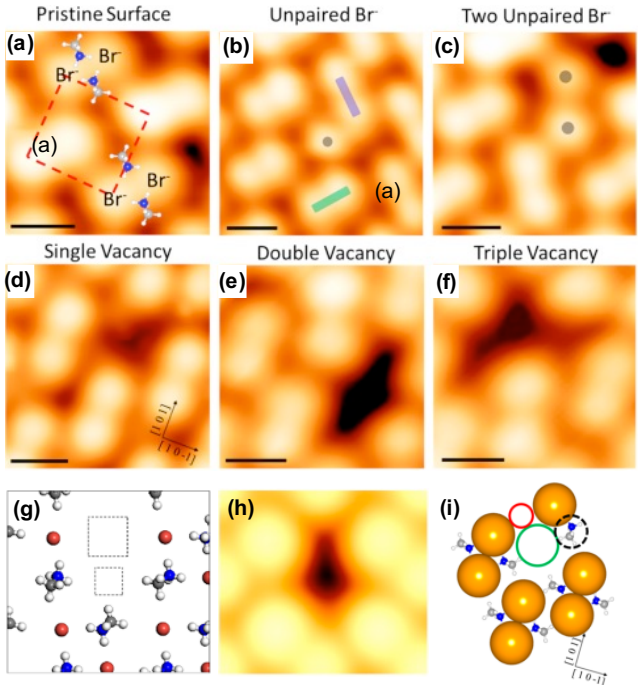

Figure 9. STM characterizations of surface defects. High-resolution STM image of (a) pristine $MAPbBr_3$ perovskite with MA^+ overlaid to show the relative position (16 × 16 Å^2, U = −9.0 V and I = 20 pA), (b) an unpaired Br anion defect (20 × 20 Å^2, U = −9.0 V and I = 20 pA), (c) two adjacent unpaired Br anion defects with a vacancy (18 × 18 Å^2, U = −9.0 V and I = 20 pA), (d) a single vacancy defect (18 × 18 Å^2, U = −3.0 V and I = 100 pA), (e) double vacancy defects (17 × 17 Å^2, U = −9.0 V and I = 20 pA) and (f) triple vacancy defects (16 × 16 Å^2, U = −9.0 V and I = 20 pA). Panels (a-f) were reproduced with permission from Ref.[18f]. Copyright 2019 American Chemical Society. (g) Calculated model of a MABr vacancy. The squares show the position of the missing Br and MA ions. Color code: N (blue), C (gray), H (white), Br (brown). (h) Simulated STM image of a MABr vacancy. The STM image was calculated for a W (111) tip. Panels (g,h) were reproduced with permission from Ref.[23f]. Copyright 2017 American Chemical Society. (i) The model slab for a single vacancy defect. Color code: N (blue), C (gray), H (white), Br (brown). Reproduced with permission from Ref.[18f]. Copyright 2019 American Chemical Society.

3.5. Halide substitution and its impact on surface stability

The poor stability of MHPMs is one of the key influencing factors that hinder their commercialization.[63] As mentioned above, the incorporation of a small amount of chlorine in MHPMs can enhance their performance mainly based on solar cell device studies.[34d-h, 35-38] However, a comprehensive understanding about the exact role of incorporated Cl remains elusive.[34f, 39, 64] STM studies offer deeper insights into the determination of the role of halogen in the mixed halide perovskites. Qi and coworkers conducted STM characterizations to determine the exact locations of deposited I^- and Cl^- ions on the surface of $MAPbBr_{3-y}I_y$ and $MAPbBr_{3-z}Cl_z$ perovskites.[18i] The evaporation of PbI_2 may produce Pb, I and PbI_2 molecules.[18n] DFT calculations simulated a variety of scenarios and revealed that the most energetically favorable was the substitution of Br anions by halide anions of I or Cl at surface of perovskites. Cl anions preferred to form isolated Cl-Br pairs rather than the single Cl-Cl pairs. A similar trend was also found in the substitution behavior for I anions, which was consistent with the STM observations of randomly distributed anion substitution. Based on the STM observations and DFT calculations, the substitution process can be described as the evaporated PbI_2 (or $PbCl_2$) molecules were firstly adsorbed on the perovskite surface, and then these molecules were dissociated. The substitution reaction then occurred between the halogen atoms, and the substituted atoms were diffused or desorbed on/from surface. The schematic drawing of the substitution mechanism is shown in Figure 10a. The Br ions adjacent to the defects are more likely to be substituted as they are less coordinated, where the chemical bond at the defect is weaker than that in the crystal.[65]. When the substitution ratio was less than 25%, the incorporation of Cl anions resulted in an increase of the decomposition energy, indicating that the stability of $MAPbBr_{3-z}Cl_z$ was enhanced (Figure 10b). In contrast, when the substitution ratio exceeded this threshold, the decomposition energy decreased with increasing Cl content. The increase of $MAPbBr_{3-z}Cl_z$ stability may be caused by the relatively stronger bond strength of Cl-Pb compared to that of Br-Pb.[18i] However, as the substitution ratio exceeded 25%, the strain induced by the incorporation of the Cl ions would be increased and counteract the benefit of Cl-Pb bond, leading to poor stability. The time-evolution XPS results indicated that the stability of the $MAPbBr_3$ was significantly enhanced as the surface Br ions were partially substituted by Cl ions. As shown in Figure 10c and d, $MAPbBr_{3-z}Cl_z$ with 18% Cl at the surface showed significantly higher stability than pristine $MAPbBr_3$ where the Pb(0) signal associated with the deterioration of the perovskite films emerged after 4 h of $MAPbBr_3$ storage in ultrahigh vacuum, while the Pb(0) peak emerged after 116 h for $MAPbBr_{3-z}Cl_z$. [18i]

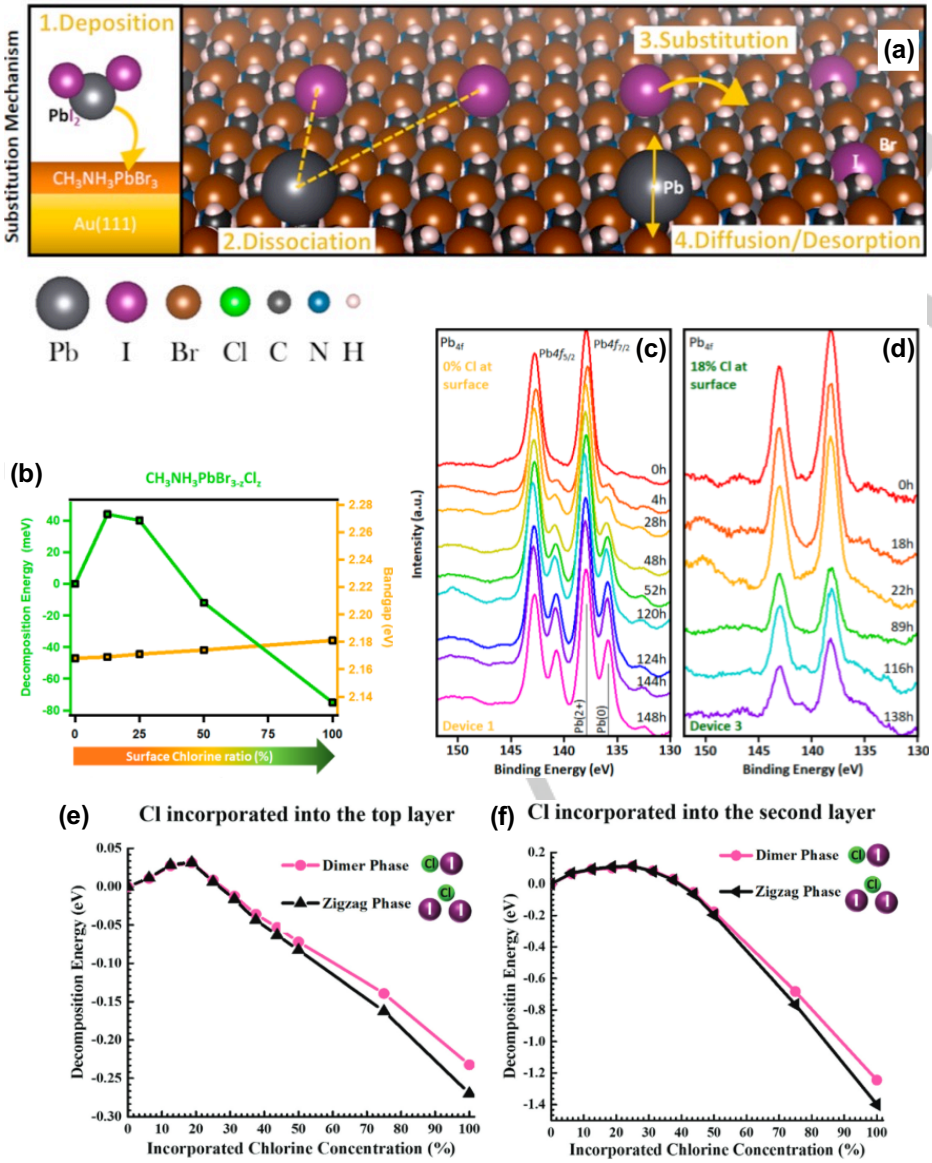

Figure 10. (a) Scheme of the substitution mechanism using PbI_2 as an example. (b) Stability versus band gap change in $MAPbBr_{3-z}Cl_z$ perovskite. The Pb 4f core-level spectra of (c) pure $MAPbBr_3$ and (d) $MAPbBr_{3-z}Cl_z$ with 18% of Cl at the surface. Panels (a-d) were reproduced with permission from Ref.[18i]. Copyright 2019 American Chemical Society. The calculated decomposition energy of (e) the first layer and (f) the second layer of $MAPbI_{3-x}Cl_x$. Panels (e,f) were reproduced with permission from Ref.[18j]. Copyright 2021 The Royal Society of Chemistry.

Similarly, incorporation of a certain amount of Cl ions into $MAPbI_3$ can enhance its stability. The optimal incorporation concentration of Cl ions was predicted to be ~18% for the topmost layer and ~25% for the second layer, respectively (see Figure 10e and f). Interestingly, the incorporation concentration into the subsurface layer is higher than that of the first layer, and the addition of Cl ions into the second layer seems to play a more important role in the stability of $MAPbI_{3-x}Cl_x$ perovskites, suggesting that the adsorbed Cl ions not only diffuse on the surface but also migrate to the interior of the bulk by means of I vacancies. The decomposition energy of $MAPbI_{3-x}Cl_x$ perovskite exhibited a non-monotonic trend of an initial increase followed by a decrease as a function of incorporated Cl concentration. These findings would have a great impact on the issue of perovskite stability, which is still one of the major challenges for the practical application of PSCs.

3.6. Atomic scale investigation on interfacial structures

Modification and engineering of interfaces is useful for MHPM applications, especially the surface topography and electronic properties of perovskite materials are highly correlated with their associated chemical and physical parameters, which can further affect the performance of the devices.[5d, 16, 59i, 66] However, the fundamental understanding of the interface science of MHPMs is still at an early stage. The relationship between interfacial properties, film structure and potential interactions has not yet been clarified. Obtaining a reliable and comprehensive picture of the interfaces would widely help to guide film processing for achieving more efficient and stable PSCs. STM can directly provide an in-depth understanding of interface properties of MHPMs through the real-space view of atomic interface and electronic structure in heterostructures. Insight into the

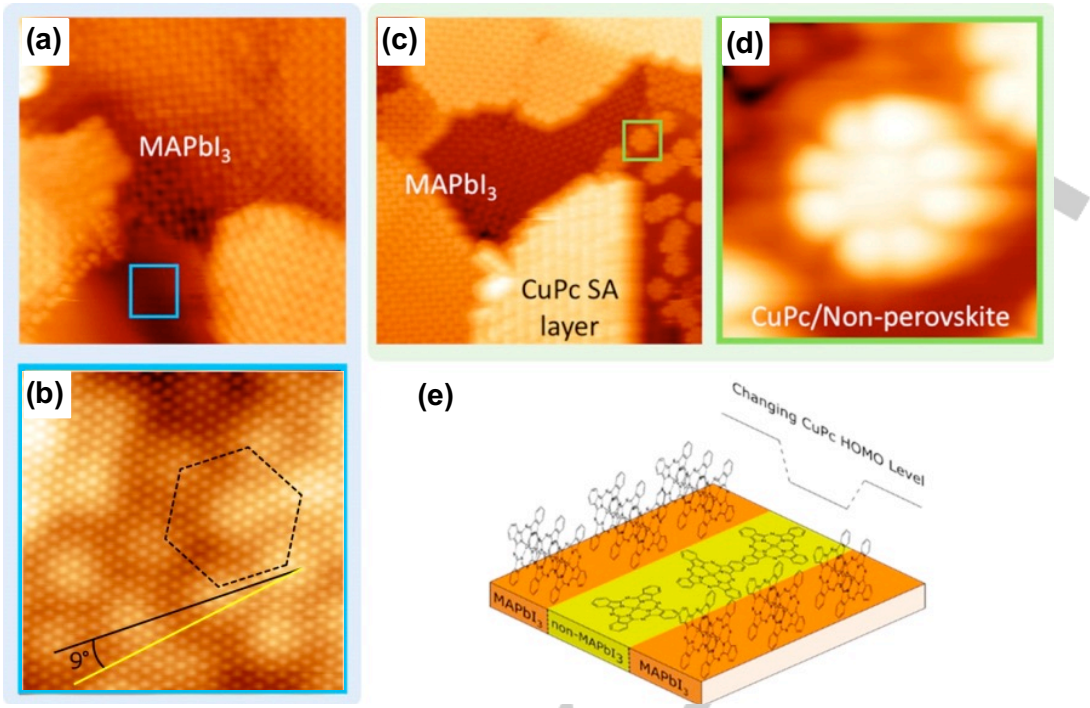

Figure 11. Interfacial structures and properties of CuPc on the non-stoichiometric MHPMs. (a) Large scale STM image showing $MAPbI_3$ and non-$MAPbI_3$ (featureless area near the blue box) domains (17.6 × 17.6 nm^2, U = −2.5 V and I = 100 pA). (b) High resolution STM of the non-$MAPbI_3$ domain showing a hexagonal superstructure (10.3 × 10.3 nm^2, U = −2.7 V and I = 300 pA). (c) CuPc deposited on the non-stoichiometric $MAPbI_3$ surface showing the different adsorption behavior (26.4 × 26.4 nm^2, U = −2.5 V and I = 100 pA). (d) Zoom-in of the face-on adsorbed CuPc on the non-$MAPbI_3$ domain (3.3 × 3.3 nm^2, U = −2.5 V and I = 100 pA). (e) Schematic diagram of the CuPc HOMO energy level change. All panels were reproduced with permission from Ref.[18k]. Copyright 2021 American Chemical Society.

fundamental properties of interfaces is essential to guide the improvement and optimization of MHPMs for optoelectronics. Recently, Qi and coworkers investigated the interface properties between $MAPbX_3$ (X = I or Br) and copper phthalocyanine (CuPc) at the atomic scale using a combination of STM and DFT calculations,[18k] where CuPc was used as the hole transport layer (HTL) material.[67] As shown in Figure 11a, the majority of the surface was covered by $MAPbI_3$ which exhibited characteristic surface reconstruction, while only a small area did not show this surface corrugation. A high resolution STM image (Figure 11b) shows a hexagonal moiré pattern with the lattice constant of 0.43 nm. This non-perovskite domain may be composed of excess precursors, either PbI_2 or iodine adlayers.[18n, 68] When the CuPc molecules were deposited onto the sample surface, these molecules formed a self-assembled layer with the *α*-polymorph structure on the $MAPbI_3$ surface, as shown in Figure 11c, where the bright striped domain can be observed in the lower middle of the image; in contrast, they adsorbed on the non-perovskite areas in a face-up orientation. The DFT calculations showed a weak interaction between CuPc and $MAPbI_3$, which further revealed the importance of intermolecular interaction in the stabilization of the CuPc self-assembled layer. A zoomed-in view (Figure 11d) showed that CuPc molecule formed a disordered flat-lying fashion on the non-$MAPbI_3$ domains, rather than forming a preferential standing configuration shown as bright stripes, suggesting a stronger interaction between CuPc and the non-perovskite material than with $MAPbI_3$. A similar result was obtained for CuPc on the $MAPbBr_3$ surface, indicating that changing the type of halide does not significantly affect the adsorption behavior of CuPc on the perovskite surface. The structural difference of CuPc on non-perovskite and perovskite material would have a significant effect on the orbital overlap at the perovskite-HTL interface.[18k] In addition, molecular orientation would strongly affect the device performance.[69] The change in the CuPc HOMO level (Figure 11e) can significantly impact the interfacial properties of the PSC, such as light absorption and interfacial charge transfer, as well as energy level alignment at the interface. The characterization of non-stoichiometric MHPMs/CuPc interface by STM at the atomic scale is an opportunity to further understanding of interfacial structure, interfacial properties, as well as the structure-interface-transport property relationship.

4. Conclusion and outlook

Even though the power conversion efficiency of PSCs has reached impressive levels, fundamental understanding of these materials is still limited, in particular the atomic-scale insights into the surface properties and their influence on device performance and stability. This article reviews the recent progress of STM studies on MHPMs to shine light on the basic surface properties of these materials. The surface structure and property studies by STM provide a deep understanding and thereby optimization of the performance of perovskite-based devices. In this review, we summarize the basic physical properties of perovskite crystal surfaces through *in situ* atomic and electronic visualizations using STM. We elucidate that the surface reconstructions of MHPMs caused two different MA^+ in-plane orientations, as well as the surface phase transition under different external stimuli. We discuss the various types of surface defects and the impact of

these defects on the properties of MHPMs. Defects are one of key factors hindering the commercialization of PSCs. We determine the role of halogen ions and the exact location of them incorporated into the perovskite crystal lattice, and also discuss that halogen ion incorporation has different effects on the electronic properties and stability of MHPMs; Another focus of this review is the discussion of electronic properties of MHPMs. We show a summary of band gap values for MHPMs prepared by different methods and on different substrates, and discuss the determinants of Fermi level positions. Some of these insights can be generalized to assist with rational design of new materials with desirable properties. As the field of PSCs is still rapidly growing, many new opportunities and challenges are ahead of us.

In the following, we outline a few new research directions that warrant further investigations.

(1) 2D halide perovskites

As the efficiency of the PSCs continues increasing, the stability of the devices has also improved significantly. Apart from the incorporation of halogen anion in the X-site approach, a new strategy stands out among many other developments, i.e., 2D MHPMs, which have a number of intriguing properties such as high-performance optoelectronics, fewer defects, suppression of anion migration and higher stability.[70] However, the fundamental properties of these 2D perovskite materials are yet to be fully understood so far. Vapor deposition methods are suitable for the synthesis and study of low-dimensional materials, and the STM technique with atomic resolution can provide a suitable platform for resolving and investigating these 2D structures. In particular, the study of surface structures, inherent defects and LDOS of 2D perovskite materials through STM/STS will provide insight into the surface properties and optoelectronic conversion-related properties.

(2) Interface properties

As discussed in Section 3.6, an in-depth understanding of the interface between perovskite and the adjacent charge transport layer is essential for rational interface engineering and further device improvement. Although it has been recognized that the interface in PSCs devices is a key to device performance and stability, dedicated interface studies are limited. STM-based techniques can provide a reliable and comprehensive picture of the interfaces between perovskites and the adjacent charge transport layers. For instance, it is possible to study the potential chemical reactions at the interface, the effects of ion migration and measure a range of electronic characteristics of interfaces including charge transport, interfacial charge transfer, energy level alignment and trap state population.

(3) Understanding the role of defects

The presence of defects has a significant impact on the stability of the MHPMs. In the case of surface reactions, the surface defects act as reaction centers, resulting in the disruption of the structure and therefore impacting charge transport. On the other hand, defects may in turn favor migration, dissociation and diffusion of ions and the substitution of halogen ions, if these phenomena are desirable for some application. Comprehensive information is lacking on the nature, density, and origin of interfacial and surface defects. Hence, more studies, especially in experiments, are required to better understand how defects affect MHPMs. STM can provide *in situ* observation of various defect types at the surface and interface of MHPMs, which will be useful for understanding of the nature of defects, charge carrier dynamics, lifetime and structural stability, and these results will help further determine the impact of defects and thus pursue appropriate strategies to improve the PCE of PSCs.

(4) Degradation

An important consideration in the practical applications is the degradation of perovskite absorbers. Degradation would lead to significant distortion of the structures or properties of the MHPMs. Suppressing the degradation reactions is an important way to improve the stability of MHPMs. To date, only a few *in situ* investigations have focused on this topic. STM allows *in situ* observation of degradation processes under a number of different external stimuli, such as exposure to oxygen, H_2O, heat and light environments. A better understanding of degradation process in MHPMs can be used to improve the performance of PSCs.

(5) Pb-free perovskites

The environmental impact of Pb in Pb-containing perovskite solar cells has led to consideration concerns. The discovery of new relevant materials to replace lead has redirected the prospects of perovskite materials. Currently, Sn-, Ge-, Sb-, and Bi-based MHPMs are considered as candidates for replacing Pb in perovskites. However, unfortunately, their applications are still limited due to their relatively low efficiency and poor stability. Therefore, it is imperative to find ways to determine the main factors that have caused the relatively low efficiencies and to develop strategies to improve the performance of Pb-free perovskites. It is expected that STM can be used to reveal numerous key parameters and novel phenomena in Pb-free perovskites, which will help Pb-free perovskites achieve high efficiency and stability, eventually enabling commercialization of Pb-free PSCs soon.

(6) Atomic-scale dynamics

MHPMs solar cells have shown extraordinary efficiencies, however, our understanding about the mechanisms of the photoelectric conversion process in perovskite solar cells is still far from complete. Dedicated conversion mechanism studies remain scarce, and the main reason is that it is very difficult to achieve high temporal resolution and atomic resolution simultaneously. The combination of STM technique with laser provides one viable solution to *in situ* probing of various atomic-scale dynamics in MHPM, such as optical absorption, photoelectric conversion, charge dynamics, electron-phonon coupling, etc.[13c, 13d, 18d, 18e, 50d, 71] With this advanced technique, it is possible to gain insights into essential understanding of internal mechanism of photovoltaic, which is of great importance for the development of PSCs, as this will provide useful guidelines for the design of high-efficiency MHPM-based photovoltaic devices.

(7) STM experiments under closer to actual solar cell operating conditions

Most of the STM studies discussed in this review were performed under ultra-high vacuum (UHV) and at low temperatures (e.g., liquid helium temperature or liquid nitrogen temperature). This is mainly because it is significantly more challenging to obtain stable STM operation *with atomic resolution* at higher temperatures and/or in the ambient air environment. On the one hand, from the fundamental understanding point of the view, it has its own right to study these interesting metal halide perovskite materials under low temperature and UHV conditions. On the other hand, to make stronger connections between STM results and actual materials under solar cell operating conditions, it will be helpful to study these materials under a condition closer to real operation conditions of solar cells. In this regard, although we have seen some promising progress,[18f, 55] more research efforts are needed.

(8) Other techniques

Indeed, STM provides fascinating opportunities to gain insights into MHPMs and has already yielded a series of exciting results. However, STM has its own limitations, i.e., it can only probe a small surface area, and this may not be sufficient to fully characterize a larger area of a perovskite solar cell. Therefore, it is necessary to combine other characterization techniques to microstructural determination for larger areas of a solar cell. MHPMs are sensitive to high-energy electron bombardment, but are more tolerant to low-energy electrons.[14c, 18e, 18o] Low-energy electron diffraction can cbe used as one of the potential candidate techniques to characterize a larger area of a perovskite solar cell.

Acknowledgements

This work was supported by funding from the Energy Materials and Surface Sciences Unit of the Okinawa Institute of Science and Technology Graduate University, the OIST R&D Cluster Research Program, the OIST Proof of Concept (POC) Program, JSPS KAKENHI Grant Number JP18K05266, and JST A-STEP Grant Number JPMJTM20HS, Japan.

Keywords: metal halide perovskite • scanning tunneling microscopy • surface chemistry • photovoltaics • electronic structure

[1] H. L. Wells, *Z. Anorg. Chem.* **1893**, *3*, 195-210.

[2] A. Kojima, K. Teshima, Y. Shirai, T. Miyasaka, *J. Am. Chem. Soc.* **2009**, *131*, 6050-6051.

[3] V. M. Goldschmidt, *Naturwissenschaften* **1926**, *14*, 477-485.

[4] aL. B. Qiu, S. S. He, L. K. Ono, Y. B. Qi, *Adv. Energy Mater.* **2020**, *10*, 1902726; bY. P. Fu, H. M. Zhu, J. Chen, M. P. Hautzinger, X. Y. Zhu, S. Jin, *Nat. Rev. Mater.* **2019**, *4*, 169-188; cW. Ke, M. G. Kanatzidis, *Nat. Commun.* **2019**, *10*, 965; dG. Q. Tong, D. Y. Son, L. K. Ono, Y. Q. Liu, Y. Q. Hu, H. Zhang, A. Jamshaid, L. B. Qiu, Z. H. Liu, Y. B. Qi, *Adv. Energy Mater.* **2021**, *11*, 2003712; eZ. H. Liu, L. B. Qiu, L. K. Ono, S. S. He, Z. H. Hu, M. W. Jiang, G. Q. Tong, Z. F. Wu, Y. Jiang, D. Y. Son, Y. Y. Dang, S. Kazaoui, Y. B. Qi, *Nat. Energy* **2020**, *5*, 596-604; fS. S. He, L. B. Qiu, L. K. Ono, Y. B. Qi, *Mater. Sci. Eng. R Rep.* **2020**, *140*, 100545; gG. Q. Tong, L. K. Ono, Y. B. Qi, *Energy Technol.* **2020**, *8*, 1900961; h J. Shamsi, A. S. Urban, M. Imran, L. De Trizio, L. Manna, *Chem. Rev.* **2019**, *119*, 3296-3348; iL. K. Ono, Y. B. Qi, S. Z. Liu, *Joule* **2018**, *2*, 1961-1990; jG. Q. Tong, M. W. Jiang, D. Y. Son, L. K. Ono, Y. B. Qi, *Adv. Funct. Mater.* **2020**, *30*, 2002526; kT. Bu, J. Li, H. Li, C. Tian, J. Su, G. Tong, L. K. Ono, C. Wang, Z. Lin, N. Chai, J. Zhang, J. Lu, j. Zhong, W. Huang, Y. B. Qi, Y. B. Chen, F. Huang, *Science* **2021**, *372*, 1327-1332.

[5] aS. D. Stranks, H. J. Snaith, *Nat. Nanotechnol.* **2015**, *10*, 391-402; bZ. F. Wu, M. W. Jiang, Z. H. Liu, A. Jamshaid, L. K. Ono, Y. B. Qi, *Adv. Energy Mater.* **2020**, *10*, 1903696; c Y. H. Lin, N. Sakai, P. Da, J. Y. Wu, H. C. Sansom, A. J. Ramadan, S. Mahesh, J. L. Liu, R. D. J. Oliver, J. Lim, L. Aspitarte, K. Sharma, P. K. Madhu, A. B. Morales-Vilches, P. K. Nayak, S. Bai, F. Gao, C. R. M. Grovenor, M. B. Johnston, J. G. Labram, J. R. Durrant, J. M. Ball, B. Wenger, B. Stannowski, H. J. Snaith, *Science* **2020**, *369*, 96-102; d R. Wang, J. J. Xue, K. L. Wang, Z. K. Wang, Y. Q. Luo, D. Fenning, G. W. Xu, S. Nuryyeva, T. Y. Huang, Y. P. Zhao, J. L. Yang, J. H. Zhu, M. H. Wang, S. Tan, I. Yavuz, K. N. Houk, Y. Yang, *Science* **2019**, *366*, 1509-1513.; eS. H. Wang, Y. Jiang, E. J. Juarez-Perez, L. K. Ono, Y. B. Qi, *Nat. Energy* **2017**, *2*, 16195; fG. Tong, D.-Y. Son, L. K. Ono, H.-B. Kang, S. He, L. Qiu, H. Zhang, Y. Liu, J. Hieulle, Y. B. Qi, *Nano Energy* **2021**, *87*, 106152; gG. Tong, L. K. Ono, Y. Liu, H. Zhang, T. Bu, Y. B. Qi, *Nano-Micro Lett.* **2021**, *13*, 155; hT. H. Wu, Z. Z. Qin, Y. B. Wang, Y. Z. Wu, W. Chen, S. F. Zhang, M. L. Cai, S. Y. Dai, J. Zhang, J. Liu, Z. M. Zhou, X. Liu, H. Segawa, H. R. Tan, Q. W. Tang, J. F. Fang, Y. W. Li, L. M. Ding, Z. J. Ning, Y. B. Qi, Y. Q. Zhang, L. Y. Han, *Nano-Micro Lett.* **2021**, *13*, 152.

[6] aK. Wang, C. C. Wu, D. Yang, Y. Y. Jiang, S. Priya, *ACS Nano* **2018**, *12*, 4919-4929; bH. P. Wang, S. Y. Li, X. Y. Liu, Z. F. Shi, X. S. Fang, J. H. He, *Adv. Mater.* **2021**, *33*, 2003309; cG. Q. Tong, M. W. Jiang, D. Y. Son, L. B. Qiu, Z. H. Liu, L. K. Ono, Y. B. Qi, *ACS Appl. Mater. Interfaces* **2020**, *12*, 14185-14194; d K. Leng, W. Fu, Y. P. Liu, M. Chhowalla, K. P. Loh, *Nat. Rev. Mater.* **2020**, *5*, 482-500.

[7] aY. Q. Liu, L. K. Ono, G. Q. Tong, H. Zhang, Y. B. Qi, *ACS Energy Lett.* **2021**, *6*, 908-914; bW. S. Yang, B. W. Park, E. H. Jung, N. J. Jeon, Y. C. Kim, D. U. Lee, S. S. Shin, J. Seo, E. K. Kim, J. H. Noh, S. I. Seok, *Science* **2017**, *356*, 1376-1379; cZ. K. Tan, R. S. Moghaddam, M. L. Lai, P. Docampo, R. Higler, F. Deschler, M. Price, A. Sadhanala, L. M. Pazos, D. Credgington, F. Hanusch, T. Bein, H. J. Snaith, R. H. Friend, *Nat. Nanotechnol.* **2014**, *9*, 687-692; dY. Q. Liu, T. L. Bu, L. K. Ono, G. Q. Tong, H. Zhang, Y. B. Qi, *Adv. Funct. Mater.* **2021**, *31*, 2103399; eY. Hassan, J. H. Park, M. L. Crawford, A. Sadhanala, J. Lee, J. C. Sadighian, E. Mosconi, R. Shivanna, E. Radicchi, M. Jeong, C. Yang, H. Choi, S. H. Park, M. H. Song, F. De Angelis, C. Y. Wong, R. H. Friend, B. R. Lee, H. J. Snaith, *Nature* **2021**, *591*, 72-77; fY. Q. Liu, L. K. Ono, Y. B. Qi, *InfoMat.* **2020**, *2*, 1095-1108.

[8] aF. Deschler, M. Price, S. Pathak, L. E. Klintberg, D. D. Jarausch, R. Higler, S. Huttner, T. Leijtens, S. D. Stranks, H. J. Snaith, M. Atature, R. T. Phillips, R. H. Friend, *J. Phys. Chem. Lett.* **2014**, *5*, 1421-1426; bL. Lei, Q. Dong, K. Gundogdu, F. So, *Adv. Funct. Mater.* **2021**, *31*, 2010144.

[9] https://www.nrel.gov/pv/assets/pdfs/best-research-cell-efficiencies.20201228.pdf. (accessed by January, 2021).

[10] aM. Saliba, T. Matsui, J. Y. Seo, K. Domanski, J. P. Correa-Baena, M. K. Nazeeruddin, S. M. Zakeeruddin, W. Tress, A. Abate, A. Hagfeldt, M. Gratzel, *Energy Environ. Sci.* **2016**, *9*, 1989-1997; bG. D. Niu, X. D. Guo, L. D. Wang, *J. Mater.*

Chem. A **2015**, *3*, 8970-8980.

[11] L. B. Qiu, S. S. He, L. K. Ono, S. Z. Liu, Y. B. Qi, *ACS Energy Lett.* **2019**, *4*, 2147-2167.

[12] aY. Jiang, L. B. Qiu, E. J. Juarez-Perez, L. K. Ono, Z. H. Hu, Z. H. Liu, Z. F. Wu, L. Q. Meng, Q. J. Wang, Y. B. Qi, *Nat. Energy* **2019**, *4*, 585-593; bA. Babayigit, A. Ethirajan, M. Muller, B. Conings, *Nat. Mater.* **2016**, *15*, 247-251.

[13] aJ. Hieulle, C. Stecker, R. Ohmann, L. K. Ono, Y. B. Qi, *Small Methods* **2018**, *2*, 1700295; bP. Schulz, D. Cahen, A. Kahn, *Chem. Rev.* **2019**, *119*, 3349-3417; cS. Sahare, P. Ghoderao, S. B. Khan, Y. Chan, S. L. Lee, *Nanoscale* **2020**, *12*, 15970-15992;dS. Wieghold, L. Nienhaus, *EcoMat.* **2021**, *3*, e12081.

[14] aC. X. Xiao, Z. Li, H. Guthrey, J. Moseley, Y. Yang, S. Wozny, H. Moutinho, B. To, J. J. Berry, B. Gorman, Y. F. Yan, K. Zhu, M. Al-Jassimt, *J. Phys. Chem. C* **2015**, *119*, 26904-26911; bN. Klein-Kedem, D. Cahen, G. Hodes, *Acc. Chem. Res.* **2016**, *49*, 347-354; cA. R. Milosavljevic, W. X. Huang, S. Sadhu, S. Ptasinska, *Angew. Chem. Int. Ed.* **2016**, *55*, 10083-10087.

[15] aW. Zhang, H. Enriquez, Y. Tong, A. Bendounan, A. Kara, A. P. Seitsonen, A. J. Mayne, G. Dujardin, H. Oughaddou, *Small* **2018**, *14*, 1804066; bW. Zhang, H. Enriquez, X. Zhang, A. J. Mayne, A. Bendounan, Y. J. Dappe, A. Kara, G. Dujardin, H. Oughaddou, *Nanotechnology* **2020**, *31*, 495602; cW. Zhang, H. Enriquez, Y. F. Tong, A. J. Mayne, A. Bendounan, Y. J. Dappe, A. Kara, G. Dujardin, H. Oughaddou, *Adv. Funct. Mater.* **2020**, *30*, 2004531; dH. Gonzalez-Herrero, J. M. Gomez-Rodriguez, P. Mallet, M. Moaied, J. J. Palacios, C. Salgado, M. M. Ugeda, J. Y. Veuillen, F. Yndurain, I. Brihuega, *Science* **2016**, *352*, 437-441; eK. Quertite, H. Enriquez, N. Trcera, Y. F. Tong, A. Bendounan, A. J. Mayne, G. Dujardin, P. Lagarde, A. El Kenz, A. Benyoussef, Y. J. Dappe, A. Kara, H. Oughaddou, *Adv. Funct. Mater.* **2021**, *31*, 2007013; fY. F. Tong, M. Bouaziz, W. Zhang, B. Obeid, A. Loncle, H. Oughaddou, H. Enriquez, K. Chaouchi, V. Esaulov, Z. S. Chen, H. Q. Xiong, Y. C. Cheng, A. Bendounan, *2D Mater.* **2020**, *7*, 035010; gH. Oughaddou, H. Enriquez, M. R. Tchalala, H. Yildirim, A. J. Mayne, A. Bendounan, G. Dujardin, M. A. Ali, A. Kara, *Prog. Surf. Sci.* **2015**, *90*, 46-83; hB. J. Feng, J. Zhang, Q. Zhong, W. B. Li, S. Li, H. Li, P. Cheng, S. Meng, L. Chen, K. H. Wu, *Nat. Chem.* **2016**, *8*, 564-569; iA. J. Mannix, X. F. Zhou, B. Kiraly, J. D. Wood, D. Alducin, B. D. Myers, X. L. Liu, B. L. Fisher, U. Santiago, J. R. Guest, M. J. Yacaman, A. Ponce, A. R. Oganov, M. C. Hersam, N. P. Guisinger, *Science* **2015**, *350*, 1513-1516.

[16] L. K. Ono, Y. B. Qi, *J. Phys. Chem. Lett.* **2016**, *7*, 4764-4794.

[17] Y. Wang, M. I. Dar, L. K. Ono, T. Y. Zhang, M. Kan, Y. W. Li, L. J. Zhang, X. T. Wang, Y. G. Yang, X. Y. Gao, Y. B. Qi, M. Gratzel, Y. X. Zhao, *Science* **2019**, *365*, 591-596.

[18] aM. Kollar, L. Ciric, J. H. Dil, A. Weber, S. Muff, H. M. Ronnow, B. Nafradi, B. P. Monnier, J. S. Luterbacher, L. Forro, E. Horvath, *Sci. Rep.* **2017**, *7*, 695; bC. Renner, G. Aeppli, B. G. Kim, Y. A. Soh, S. W. Cheong, *Nature* **2002**, *416*, 518-521; cJ. I. J. Choi, M. E. Khan, Z. Hawash, K. J. Kim, H. Lee, L. K. Ono, Y. B. Qi, Y. H. Kim, J. Y. Park, *J. Mater. Chem. A* **2019**, *7*, 20760-20766; dH. C. Hsu, B. C. Huang, S. C. Chin, C. R. Hsing, D. L. Nguyen, M. Schnedler, R. Sankar, R. E. Dunin-Borkowski, C. M. Wei, C. W. Chen, P. Ebert, Y. P. Chiu, *ACS Nano* **2019**, *13*, 4402-4409; eR. Ohmann, L. K. Ono, H. S. Kim, H. P. Lin, M. V. Lee, Y. Y. Li, N. G. Park, Y. B. Qi, *J. Am. Chem. Soc.* **2015**, *137*, 16049-16054; fC. Stecker, K. X. Liu, J. Hieulle, R. Ohmann, Z. Y. Liu, L. K. Ono, G. F. Wang, Y. B. Qi, *ACS Nano* **2019**, *13*, 12127-12136; gM. Z. Liu, M. B. Johnston, H. J. Snaith, *Nature* **2013**, *501*, 395-398; hL. K. Ono, S. H. Wang, Y. Kato, S. R. Raga, Y. B. Qi, *Energy Environ. Sci.* **2014**, *7*, 3989-3993; iJ. Hieulle, X. M. Wang, C. Stecker, D. Y. Son, L. B. Qu, R. Ohmann, L. K. Ono, A. Mugarza, Y. F. Yan, Y. B. Qi, *J. Am. Chem. Soc.* **2019**, *141*, 3515-3523; jA. Jamshaid, Z. Guo, J. Hieulle, C. Stecker, R. Ohmann, L. K. Ono, L. Qiu, G. Tong, W. Yin, Y. B. Qi, *Energy Environ. Sci.* **2021**, *14*, 4541-4554; kC. Stecker, Z. Liu, J. Hieulle, S. Zhang, L. K. Ono, G. Wang, Y. B. Qi, *ACS Nano* **2021**, Article ASAP; lL. K. Ono, M. R. Leyden, S. H. Wang, Y. B. Qi, *J. Mater. Chem. A* **2016**, *4*, 6693-6713; mL. M. She, M. Z. Liu, D. Y. Zhong, *ACS Nano* **2016**, *10*, 1126-1131; nL. M. She, M. Z. Liu, X. L. Li, Z. Y. Cai, D. Y. Zhong, *Surf. Sci.* **2017**, *656*, 17-23; oJ. Hieulle, S. L. Luo, D. Y. Son, A. Jamshaid, C. Stecker, Z. H. Liu, G. R. Na, D. W. Yang, R. Ohmann, L. K. Ono, L. J. Zhang, Y. B. Qi, *J. Phys. Chem. Lett.* **2020**, *11*, 818-823; pM. Sessolo, C. Momblona, L. Gil-Escrig, H. J. Bolink, *MRS Bull.* **2015**, *40*, 660-666; qB. Stoger, M. Hieckel, F. Mittendorfer, Z. M. Wang, D. Fobes, J. Peng, Z. Q. Mao, M. Schmid, J. Redinger, U. Diebold, *Phys. Rev. Lett.* **2014**, *113*, 116101; rJ. Li, R. R. Gao, F. Gao, J. Lei, H. X. Wang, X. Wu, J. B. Li, H. Liu, X. D. Hua, S. Z. Liu, *J. Alloys Compd.* **2020**, *818*, 152903.

[19] aS. J. Pearton, J. C. Yang, P. H. Cary, F. Ren, J. Kim, M. J. Tadjer, M. A. Mastro, *Applied Physics Reviews* **2018**, *5*, 011301; bY. Hirsh, S. Gorfman, D. Shermana, *Acta Mater.* **2020**, *193*, 338-349; cJ. Lee, T. Y. Ko, J. H. Kim, H. Bark, B. Kang, S. G. Jung, T. Park, Z. Lee, S. Ryu, C. Lee, *ACS Nano* **2017**, *11*, 10935-10944.

[20] K. S. Novoselov, D. Jiang, F. Schedin, T. J. Booth, V. V. Khotkevich, S. V. Morozov, A. K. Geim, *Proc. Natl. Acad. Sci. U. S. A.* **2005**, *102*, 10451-10453.

[21] M. Kollar, L. Ciric, J. H. Dil, A. Weber, S. Muff, H. M. Ronnow, B. Nafradi, B. P. Monnier, J. S. Luterbacher, L. Forro, E. Horvath, *Sci. Rep.* **2017**, *7*.

[22] B. Stoger, M. Hieckel, F. Mittendorfer, Z. M. Wang, M. Schmid, G. S. Parkinson, D. Fobes, J. Peng, J. E. Ortmann, A. Limbeck, Z. Q. Mao, J. Redinger, U. Diebold, *Phys. Rev. B* **2014**, *90*, 165438.

[23] aW. M. Ming, S. Y. Chen, M. H. Du, *J. Mater. Chem. A* **2016**, *4*, 16975-16981; bY. H. Kye, C. J. Yu, U. G. Jong, Y. Chen, A. Walsh, *J. Phys. Chem. Lett.* **2018**, *9*, 2196-2201; cD. Meggiolaro, F. De Angelis, *ACS Energy Lett.* **2018**, *3*, 2206-2222; dA. Walsh, D. O. Scanlon, S. Y. Chen, X. G. Gong, S. H. Wei, *Angew. Chem. Int. Ed.* **2015**, *54*, 1791-1794; eW. J. Yin, T. T. Shi, Y. F. Yan, *Adv. Mater.* **2014**, *26*, 4653-4658; fY. Liu, K. Palotas, X. Yuan, T. Hou, H. Lin, Y. Li, S. T. Lee, *ACS Nano* **2017**, *11*, 2060-2065.

[24] aC. Celebi, O. Ari, R. T. Senger, *Phys. Rev. B* **2013**, *87*, 085308; bW. Mayr-Schmolzer, D. Halwidl, F. Mittendorfer, M. Schmid, U. Diebold, J. Redinger, *Surf. Sci.* **2019**, *680*, 18-23.

[25] A. Poglitsch, D. Weber, *J. Chem. Phys.* **1987**, *87*, 6373-6378.

[26] C. R. Henry, *Surf. Sci. Rep.* **1998**, *31*, 235-325.

[27] aA. Kubono, R. Akiyama, *J. Appl. Phys.* **2005**, *98*, 093502; bZ. J. Liu, P. W. Shum, Y. G. Shen, *Appl. Phys. Lett.* **2005**, *86*, 251908.

[28] T. G. Kim, S. W. Seo, H. Kwon, J. Hahn, J. W. Kim, *Phys. Chem. Chem. Phys.* **2015**, *17*, 24342-24348.

[29] T. Baikie, Y. N. Fang, J. M. Kadro, M. Schreyer, F. X. Wei, S. G. Mhaisalkar, M. Graetzel, T. J. White, *J. Mater. Chem. A* **2013**, *1*, 5628-5641.

[30] L. Gil-Escrig, C. Momblona, M. G. La-Placa, P. P. Boix, M. Sessolo, H. J. Bolink, *Adv. Energy Mater.* **2018**, *8*, 1703506.

[31] aY. F. Wang, J. Wu, P. Zhang, D. T. Liu, T. Zhang, L. Ji, X. L. Gu, Z. D. Chen, S. B. Li, *Nano Energy* **2017**, *39*, 616-625; bX. Y. Wu, Y. Jiang, C. Chen, J. L. Guo, X. Y. Kong, Y. C. Feng, S. J. Wu, X. S. Gao, X. B. Lu, Q. M. Wang, G. F. Zhou, Y. W. Chen, J. M. Liu, K. Kempa, J. W. Gao, *Adv. Funct. Mater.* **2020**, *30*, 1908613.

[32] aC. Quarti, F. De Angelis, D. Beljonne, *Chem. Mater.* **2017**,

29, 958-968; bA. Torres, L. G. C. Rego, *J. Phys. Chem. C* **2014**, *118*, 26947-26954; cJ. Haruyama, K. Sodeyama, L. Y. Han, Y. Tateyama, *J. Phys. Chem. Lett.* **2014**, *5*, 2903-2909; dY. Wang, B. G. Sumpter, J. S. Huang, H. M. Zhang, P. R. Liu, H. G. Yang, H. J. Zhao, *J. Phys. Chem. C* **2015**, *119*, 1136-1145.

[33] H. Mashiyama, Y. Kawamura, Y. Kubota, *J. Korean Phys. Soc.* **2007**, *51*, 850-853.

[34] aE. T. Hoke, D. J. Slotcavage, E. R. Dohner, A. R. Bowring, H. I. Karunadasa, M. D. McGehee, *Chem. Sci.* **2015**, *6*, 613-617; bA. J. Knight, L. M. Herz, *Energy Environ. Sci.* **2020**, *13*, 2024-2046; cP. Nandi, C. Giri, D. Swain, U. Manju, S. D. Mahanti, D. Topwal, *ACS Appl. Energy Mater.* **2018**, *1*, 3807-3814; dF. Y. Jiang, Y. G. Rong, H. W. Liu, T. F. Liu, L. Mao, W. Meng, F. Qin, Y. Y. Jiang, B. W. Luo, S. X. Xiong, J. H. Tong, Y. Liu, Z. F. Li, H. W. Han, Y. H. Zhou, *Adv. Funct. Mater.* **2016**, *26*, 8119-8127; eJ. Liu, O. V. Prezhdo, *J. Phys. Chem. Lett.* **2015**, *6*, 4463-4469; fH. Yu, F. Wang, F. Y. Xie, W. W. Li, J. Chen, N. Zhao, *Adv. Funct. Mater.* **2014**, *24*, 7102-7108; gQ. Chen, H. P. Zhou, Y. H. Fang, A. Z. Stieg, T. B. Song, H. H. Wang, X. B. Xu, Y. S. Liu, S. R. Lu, J. B. You, P. Y. Sun, J. McKay, M. S. Goorsky, Y. Yang, *Nat. Commun.* **2015**, *6*, 7269; hC. Quarti, E. Mosconi, P. Umari, F. De Angelis, *Inorg. Chem.* **2017**, *56*, 74-83.

[35] aM. M. Lee, J. Teuscher, T. Miyasaka, T. N. Murakami, H. J. Snaith, *Science* **2012**, *338*, 643-647; bN. J. Jeon, J. H. Noh, Y. C. Kim, W. S. Yang, S. Ryu, S. I. Seok, *Nat. Mater.* **2014**, *13*, 897-903.

[36] M. Zhang, H. Yu, M. Q. Lyu, Q. Wang, J. H. Yun, L. Z. Wang, *Chem. Commun.* **2014**, *50*, 11727-11730.

[37] aE. Edri, S. Kirmayer, D. Cahen, G. Hodes, *J. Phys. Chem. Lett.* **2013**, *4*, 897-902; bE. Edri, S. Kirmayer, M. Kulbak, G. Hodes, D. Cahen, *J. Phys. Chem. Lett.* **2014**, *5*, 429-433.

[38] aS. Colella, E. Mosconi, G. Pellegrino, A. Alberti, V. L. P. Guerra, S. Masi, A. Listorti, A. Rizzo, G. G. Condorelli, F. De Angelis, G. Gigli, *J. Phys. Chem. Lett.* **2014**, *5*, 3532-3538; bE. Mosconi, E. Ronca, F. De Angelis, *J. Phys. Chem. Lett.* **2014**, *5*, 2619-2625; cA. J. Yost, A. Pimachev, C. C. Ho, S. B. Darling, L. Wang, W. F. Su, Y. Dahnovsky, T. Y. Chien, *ACS Appl. Mater. Interfaces* **2016**, *8*, 29110-29116.

[39] aL. K. Ono, E. J. Juarez-Perez, Y. B. Qi, *ACS Appl. Mater. Interfaces* **2017**, *9*, 30197-30246; bY. Y. Zhou, Z. M. Zhou, M. Chen, Y. X. Zong, J. S. Huang, S. P. Pang, N. P. Padture, *J. Mater. Chem. A* **2016**, *4*, 17623-17635; cW. J. Yin, J. H. Yang, J. Kang, Y. F. Yan, S. H. Wei, *J. Mater. Chem. A* **2015**, *3*, 8926-8942.

[40] S. Colella, E. Mosconi, P. Fedeli, A. Listorti, F. Gazza, F. Orlandi, P. Ferro, T. Besagni, A. Rizzo, G. Calestani, G. Gigli, F. De Angelis, R. Mosca, *Chem. Mater.* **2013**, *25*, 4613-4618.

[41] J. Chae, Q. F. Dong, J. S. Huang, A. Centrone, *Nano Lett.* **2015**, *15*, 8114-8121.

[42] aM. Kulbak, D. Cahen, G. Hodes, *J. Phys. Chem. Lett.* **2015**, *6*, 2452-2456; bJ. Chen, D. J. Morrow, Y. P. Fu, W. H. Zheng, Y. Z. Zhao, L. N. Dang, M. J. Stolt, D. D. Kohler, X. X. Wang, K. J. Czech, M. P. Hautzinger, S. H. Shen, L. J. Guo, A. L. Pan, J. C. Wright, S. Jin, *J. Am. Chem. Soc.* **2017**, *139*, 13525-13532.

[43] A. S. Thind, G. F. Luo, J. A. Hachtel, M. V. Morrell, S. B. Cho, A. Y. Borisevich, J. C. Idrobo, Y. C. Xing, R. Mishra, *Adv. Mater.* **2019**, *31*, 1805047.

[44] Y. Yang, C. J. Hou, T. X. Liang, *Phys. Chem. Chem. Phys.* **2021**, *23*, 7145-7152.

[45] J. Endres, D. A. Egger, M. Kulbak, R. A. Kerner, L. F. Zhao, S. H. Silver, G. Hodes, B. P. Rand, D. Cahen, L. Kronik, A. Kahn, *J. Phys. Chem. Lett.* **2016**, *7*, 2722-2729.

[46] aE. M. Miller, Y. X. Zhao, C. C. Mercado, S. K. Saha, J. M. Luther, K. Zhu, V. Stevanovic, C. L. Perkins, J. van de Lagemaat, *Phys. Chem. Chem. Phys.* **2014**, *16*, 22122-22130; bP. Schulz, L. L. Whittaker-Brooks, B. A. MacLeod, D. C. Olson, Y. L. Loo, A. Kahn, *Adv. Mater. Interfaces* **2015**, *2*, 1400532; cT. Gattet, D. Grabowski, T. Kirchartz, A. Redinger, *Nanoscale* **2019**, *11*, 16828-16836; dS. X. Tao, I. Schmidt, G. Brocks, J. K. Jiang, I. Tranca, K. Meerholz, S. Olthof, *Nat. Commun.* **2019**, *10*, 2560.

[47] D. Niesner, M. Wilhelm, I. Levchuk, A. Osvet, S. Shrestha, M. Batentschuk, C. Brabec, T. Fauster, *Phys. Rev. Lett.* **2016**, *117*, 126401.

[48] X. Y. Che, B. Traore, C. Katan, M. Kepenekian, J. Even, *Phys. Chem. Chem. Phys.* **2018**, *20*, 9638-9643.

[49] X. Z. Zhou, Z. Y. Zhang, *AIP Adv.* **2020**, *10*, 085210.

[50] aF. S. Zu, P. Amsalem, D. A. Egger, R. B. Wang, C. M. Wolff, H. H. Fang, M. A. Loi, D. Neher, L. Kronik, S. Duhm, N. Koch, *J. Phys. Chem. Lett.* **2019**, *10*, 601-609; bP. Schulz, E. Edri, S. Kirmayer, G. Hodes, D. Cahen, A. Kahn, *Energy Environ. Sci.* **2014**, *7*, 1377-1381; cD. Azulay, I. Levine, S. Gupta, E. Barak-Kulbak, A. Bera, G. San, S. Simha, D. Cahen, O. Millo, G. Hodes, I. Balberg, *Phys. Chem. Chem. Phys.* **2018**, *20*, 24444-24452; dM. C. Shih, S. S. Li, C. H. Hsieh, Y. C. Wang, H. D. Yang, Y. P. Chiu, C. S. Chang, C. W. Chen, *Nano Lett.* **2017**, *17*, 1154-1160; eX. L. Liu, C. G. Wang, L. Lyu, C. C. Wang, Z. G. Xiao, C. Bi, J. S. Huang, Y. L. Gao, *Phys. Chem. Chem. Phys.* **2015**, *17*, 896-902; fH. Kawai, G. Giorgi, A. Marini, K. Yamashita, *Nano Lett.* **2015**, *15*, 3103-3108; gR. Lindblad, D. Q. Bi, B. W. Park, J. Oscarsson, M. Gorgoi, H. Siegbahn, M. Odelius, E. M. J. Johansson, H. Rensmo, *J. Phys. Chem. Lett.* **2014**, *5*, 648-653; hJ. E. Castellanos-Aguila, L. Lodeiro, E. Menendez-Proupin, A. L. Montero-Alejo, P. Palacios, J. C. Conesa, P. Wahnon, *ACS Appl. Mater. Interfaces* **2020**, *12*, 44648-44657; iB. J. Foley, D. L. Marlowe, K. Y. Sun, W. A. Saidi, L. Scudiero, M. C. Gupta, J. J. Choi, *Appl. Phys. Lett.* **2015**, *106*, 243904; jW. H. Guan, Y. Li, Q. X. Zhong, H. Y. Liu, J. N. Chen, H. C. Hu, K. X. Lv, J. Gong, Y. Xu, Z. H. Kang, M. H. Cao, Q. Zhang, *Nano Lett.* **2021**, *21*, 597-604; kY. Yang, T. Chen, D. Q. Pan, J. Gao, C. T. Zhu, F. Y. Lin, C. H. Zhou, Q. D. Tai, S. Xiao, Y. B. Yuan, Q. L. Dai, Y. B. Han, H. P. Xie, X. Y. Guo, *Nano Energy* **2020**, *67*, 104246; lG. S. H. Thien, N. A. Talik, B. K. Yap, H. Nakajima, S. Tunmee, N. Chanlek, B. T. Goh, *Ceram. Int.* **2020**, *46*, 29041-29051.

[51] Y. Yamada, T. Nakamura, M. Endo, A. Wakamiya, Y. Kanemitsu, *J. Am. Chem. Soc.* **2014**, *136*, 11610-11613.

[52] aY. L. Li, W. H. Sun, W. B. Yan, S. Y. Ye, H. T. Peng, Z. W. Liu, Z. Q. Bian, C. H. Huang, *Adv. Funct. Mater.* **2015**, *25*, 4867-4873; bY. J. Fang, Q. F. Dong, Y. C. Shao, Y. B. Yuan, J. S. Huang, *Nat. Photonics* **2015**, *9*, 679-686.

[53] J. Hieulle, S. Luo, D.-Y. Son, A. Jamshaid, C. Stecker, Z. Liu, G. Na, D. Yang, R. Ohmann, L. K. Ono, *J. Phys. Chem. Lett.* **2020**, *11*, 818-823.

[54] aX. Liu, Z. Luo, W. X. Yin, A. P. Litvin, A. V. Baranov, J. Q. Zhang, W. Y. Liu, X. Y. Zhang, W. T. Zheng, *Nanoscale Adv.* **2020**, *2*, 1973-1979; bY. Lu, Q. Han, Y. Zhao, D. D. Xie, J. H. Wei, P. Yuan, C. G. Yang, Y. Z. Li, X. L. Liu, Y. L. Gao, *Results Phys.* **2020**, *17*, 103087; cJ. Endres, M. Kulbak, L. F. Zhao, B. P. Rand, D. Cahen, G. Hodes, A. Kahn, *J. Appl. Phys.* **2017**, *121*, 035304.

[55] S. Wieghold, N. Shirato, V. Rose, L. Nienhaus, *J. Appl. Phys.* **2020**, *128*, 125303.

[56] N. Kedem, M. Kulbak, T. M. Brenner, G. Hodes, D. Cahen, *Phys. Chem. Chem. Phys.* **2017**, *19*, 5753-5762.

[57] aJ. M. Frost, K. T. Butler, F. Brivio, C. H. Hendon, M. van Schilfgaarde, A. Walsh, *Nano Lett.* **2014**, *14*, 2584-2590; bA. M. A. Leguy, J. M. Frost, A. P. McMahon, V. G. Sakai, W. Kockelmann, C. H. Law, X. E. Li, F. Foglia, A. Walsh, B. C. O'Regan, J. Nelson, J. T. Cabral, P. R. F. Barnes, *Nat. Commun.* **2015**, *6*, 7124.

[58] N. Li, L. Song, Y. H. Jia, Y. F. Dong, F. Y. Xie, L. D. Wang, S. X. Tao, N. Zhao, *Adv. Mater.* **2020**, *32*, 1907786.

[59] aY. H. Shao, Z. G. Xiao, C. Bi, Y. B. Yuan, J. S. Huang, *Nat.*

Commun. **2014**, *5*, 5784; bD. W. Miller, G. E. Eperon, E. T. Roe, C. W. Warren, H. J. Snaith, M. C. Lonergan, *Appl. Phys. Lett.* **2016**, *109*, 153902; cZ. H. Liu, J. N. Hu, H. Y. Jiao, L. Li, G. H. J. Zheng, Y. H. Chen, Y. Huang, Q. Zhang, C. Shen, Q. Chen, H. P. Zhou, *Adv. Mater.* **2017**, *29*, 1606774; dJ. M. Ball, A. Petrozza, *Nat. Energy* **2016**, *1*, 1-13; eA. Maiti, S. Chatterjee, L. Peedikakkandy, A. J. Pal, *Sol. RRL* **2020**, *4*, 2000505; fL. Qiao, W. H. Fang, R. Long, O. V. Prezhdo, *Angew. Chem. Int. Ed.* **2020**, *59*, 4684-4690; gX. Zhang, M. E. Turiansky, C. G. Van de Walle, *J. Phys. Chem. C* **2020**, *124*, 6022-6027; hT. Leijtens, G. E. Eperon, A. J. Barker, G. Grancini, W. Zhang, J. M. Ball, A. R. S. Kandada, H. J. Snaith, A. Petrozza, *Energy Environ. Sci.* **2016**, *9*, 3472-3481; iL. K. Ono, S. Z. Liu, Y. B. Qi, *Angew. Chem. Int. Ed.* **2020**, *59*, 6676-6698; jD. W. deQuilettes, S. M. Vorpahl, S. D. Stranks, H. Nagaoka, G. E. Eperon, M. E. Ziffer, H. J. Snaith, D. S. Ginger, *Science* **2015**, *348*, 683-686.

[60] aW. J. Yin, T. T. Shi, Y. F. Yan, *Appl. Phys. Lett.* **2014**, *104*, 063903; bD. Meggiolaro, S. G. Motti, E. Mosconi, A. J. Barker, J. Ball, C. A. R. Perini, F. Deschler, A. Petrozza, F. De Angelis, *Energy Environ. Sci.* **2018**, *11*, 702-713.

[61] H. S. Duan, H. P. Zhou, Q. Chen, P. Y. Sun, S. Luo, T. B. Song, B. Bob, Y. Yang, *Phys. Chem. Chem. Phys.* **2015**, *17*, 112-116.

[62] aN. Aristidou, I. Sanchez-Molina, T. Chotchuangchutchaval, M. Brown, L. Martinez, T. Rath, S. A. Haque, *Angew. Chem. Int. Ed.* **2015**, *54*, 8208-8212; bN. Z. Koocher, D. Saldana-Greco, F. G. Wang, S. Liu, A. M. Rappe, *J. Phys. Chem. Lett.* **2015**, *6*, 4371-4378; cE. Mosconi, J. M. Azpiroz, F. De Angelis, *Chem. Mater.* **2015**, *27*, 4885-4892; dN. Aristidou, C. Eames, I. Sanchez-Molina, X. N. Bu, J. Kosco, M. S. Islam, S. A. Haque, *Nat. Commun.* **2017**, *8*, 15218.

[63] aJ. H. Noh, S. H. Im, J. H. Heo, T. N. Mandal, S. I. Seok, *Nano Lett.* **2013**, *13*, 1764-1769; bK. A. Bush, A. F. Palmstrom, Z. S. J. Yu, M. Boccard, R. Cheacharoen, J. P. Mailoa, D. P. McMeekin, R. L. Z. Hoye, C. D. Bailie, T. Leijtens, I. M. Peters, M. C. Minichetti, N. Rolston, R. Prasanna, S. Sofia, D. Harwood, W. Ma, F. Moghadam, H. J. Snaith, T. Buonassisi, Z. C. Holman, S. F. Bent, M. D. McGehee, *Nat. Energy* **2017**, *2*, 17009; cQ. Jing, M. Zhang, X. Huang, X. M. Ren, P. Wang, Z. D. Lu, *Nanoscale* **2017**, *9*, 7391-7396; dC. Park, H. Ko, D. H. Sin, K. C. Song, K. Cho, *Adv. Funct. Mater.* **2017**, *27*, 1703546; eN. R. Poespawati, J. Sulistianto, T. Abuzairi, R. W. Purnamaningsih, *Int. J. Photoenergy* **2020**, *2020*, 8827917; fH. R. Tan, A. Jain, O. Voznyy, X. Z. Lan, F. P. G. de Arquer, J. Z. Fan, R. Quintero-Bermudez, M. J. Yuan, B. Zhang, Y. C. Zhao, F. J. Fan, P. C. Li, L. N. Quan, Y. B. Zhao, Z. H. Lu, Z. Y. Yang, S. Hoogland, E. H. Sargent, *Science* **2017**, *355*, 722-726; gJ. B. You, L. Meng, T. B. Song, T. F. Guo, Y. Yang, W. H. Chang, Z. R. Hong, H. J. Chen, H. P. Zhou, Q. Chen, Y. S. Liu, N. De Marco, Y. Yang, *Nat. Nanotechnol.* **2016**, *11*, 75-81.

[64] aM. D. Ye, X. D. Hong, F. Y. Zhang, X. Y. Liu, *J. Mater. Chem. A* **2016**, *4*, 6755-6771; bV. L. Pool, A. Gold-Parker, M. D. McGehee, M. F. Toney, *Chem. Mater.* **2015**, *27*, 7240-7243; cS. Q. Luo, W. A. Daoud, *Materials* **2016**, *9*, 123; dT. Y. Zhang, M. J. Yang, E. E. Benson, Z. J. Li, J. van de Lagemaat, J. M. Luther, Y. F. Yan, K. Zhu, Y. X. Zhao, *Chem. Commun.* **2015**, *51*, 7820-7823; eJ. J. Ma, M. C. Qin, Y. H. Li, X. Wu, Z. T. Qin, Y. C. Wu, G. J. Fang, X. H. Lu, *Matter* **2021**, *4*, 313-327; fD. Vidyasagar, Y. H. Yun, S. Shin, J. Jung, W. Park, J. W. Lee, G. S. Han, C. Ko, S. Lee, *Materials* **2021**, *14*, 1102.

[65] Y. Lin, Y. Bai, Y. J. Fang, Z. L. Chen, S. Yang, X. P. Zheng, S. Tang, Y. Liu, J. J. Zhao, J. S. Huang, *J. Phys. Chem. Lett.* **2018**, *9*, 654-658.

[66] aQ. Jiang, Y. Zhao, X. W. Zhang, X. L. Yang, Y. Chen, Z. M. Chu, Q. F. Ye, X. X. Li, Z. G. Yin, J. B. You, *Nat. Photonics* **2019**, *13*, 460-466; bE. Aydin, M. De Bastiani, S. De Wolf, *Adv. Mater.* **2019**, *31*, 1900428; cE. H. Jung, N. J. Jeon, E. Y. Park, C. S. Moon, T. J. Shin, T. Y. Yang, J. H. Noh, J. Seo, *Nature* **2019**, *567*, 511-515; dH. P. Zhou, Q. Chen, G. Li, S. Luo, T. B. Song, H. S. Duan, Z. R. Hong, J. B. You, Y. S. Liu, Y. Yang, *Science* **2014**, *345*, 542-546; eQ. S. Dong, C. Zhu, M. Chen, C. Jiang, J. Y. Guo, Y. L. Feng, Z. H. Dai, S. K. Yadavalli, M. Y. Hu, X. Cao, Y. Q. Li, Y. Z. Huang, Z. Liu, Y. T. Shi, L. D. Wang, N. P. Padture, Y. Y. Zhou, *Nat. Commun.* **2021**, *12*, 973; fZ. H. Dai, S. K. Yadavalli, M. Chen, A. Abbaspourtamijani, Y. Qi, N. P. Padture, *Science* **2021**, *372*, 618-622; gY. M. Chen, Y. S. Lei, Y. H. Li, Y. G. Yu, J. Z. Cai, M. H. Chiu, R. Rao, Y. Gu, C. F. Wang, W. J. Choi, H. J. Hu, C. H. Wang, Y. Li, J. W. Song, J. X. Zhang, B. Y. Qi, M. Y. Lin, Z. R. Zhang, A. E. Islam, B. Maruyama, S. Dayeh, L. J. Li, K. S. Yang, Y. H. Lo, S. Xu, *Nature* **2020**, *577*, 209-215; hD. Kim, H. J. Jung, I. J. Park, B. W. Larson, S. P. Dunfield, C. X. Xiao, J. Kim, J. H. Tong, P. Boonmongkolras, S. G. Ji, F. Zhang, S. R. Pae, M. Kim, S. B. Kang, V. Dravid, J. J. Berry, J. Y. Kim, K. Zhu, D. H. Kim, B. Shin, *Science* **2020**, *368*, 155-160; iL. B. Qiu, L. K. Ono, Y. Jiang, M. R. Leyden, S. R. Raga, S. H. Wang, Y. B. Qi, *J. Phys. Chem. B* **2018**, *122*, 511-520; jZ. F. Wu, M. W. Jiang, Z. H. Liu, A. Jamshaid, L. K. Ono, Y. B. Qi, *Adv. Energy Mater.* **2020**, *10*.

[67] F. G. Zhang, X. C. Yang, M. Cheng, W. H. Wang, L. C. Sun, *Nano Energy* **2016**, *20*, 108-116.

[68] aC. H. Yang, S. L. Yau, L. J. Fan, Y. W. Yang, *Surf. Sci.* **2003**, *540*, 274-284; bW. Haiss, J. K. Sass, X. Gao, M. J. Weaver, *Surf. Sci.* **1992**, *274*, L593-L598; cX. P. Gao, M. J. Weaver, *J. Am. Chem. Soc.* **1992**, *114*, 8544-8551.

[69] W. Chen, D. C. Qi, H. Huang, X. Y. Gao, A. T. S. Wee, *Adv. Funct. Mater.* **2011**, *21*, 410-424.

[70] aD. H. Cao, C. C. Stoumpos, O. K. Farha, J. T. Hupp, M. G. Kanatzidis, *J. Am. Chem. Soc.* **2015**, *137*, 7843-7850; bI. C. Smith, E. T. Hoke, D. Solis-Ibarra, M. D. McGehee, H. I. Karunadasa, *Angew. Chem. Int. Ed.* **2014**, *53*, 11232-11235; cM. I. Saidaminov, O. F. Mohammed, O. M. Bakr, *ACS Energy Lett.* **2017**, *2*, 889-896; dAkriti, E. Z. Shi, S. B. Shiring, J. Q. Yang, C. L. Atencio-Martinez, B. Yuan, X. C. Hu, Y. Gao, B. P. Finkenauer, A. J. Pistone, Y. Yu, P. L. Liao, B. M. Savoie, L. T. Dou, *Nat. Nanotechnol.* **2021**, *16*, 584-591.

[71] R. Gutzler, M. Garg, C. R. Ast, K. Kuhnke, K. Kern, *Nat. Rev. Phys.* **2021**, *3*, 441-453.

Entry for the Table of Contents

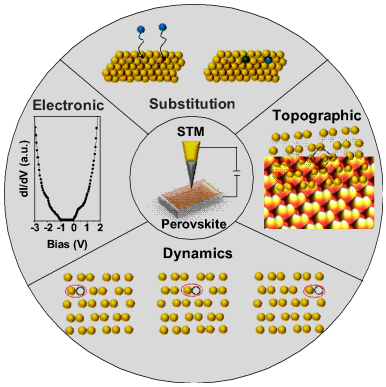

STM/STS is a powerful technique to visualize the topographic and electronic structures of perovskite with atomic-level resolution. This technique can also be used to reveal surface defect dynamics, charge carrier dynamics, on-surface reaction and optoelectronic properties at the surface and interfaces of perovskite.